N88-15778

VON KARMAN INSTITUTE FOR FLUID DYNAMICS

LECTURE SERIES 1987-03

INFLUENCE OF ENVIRONMENTAL FACTORS ON AIRCRAFT WING PERFORMANCE

FEBRUARY 16 - 20, 1987

EFFECTS OF ENVIRONMENTALLY IMPOSED ROUGHNESS ON AIRFOIL PERFORMANCE

TUNCER CEBECI

DOUGLAS AIRCRAFT CO, USA

1.0 Introduction

Considerable care is taken in the design and construction of wings to ensure that the shape provides the required combination of lift and drag over the flight cycle and that the surface is aerodynamically smooth. The presence of rain, insect deposits or ice can change the shape of the wing and its surface finish and this paper examines the magnitude of the effects on lift and drag and describes the status of calculation methods which can provide a basic tool for their prediction.

The problems associated with flying airplanes through heavy rain include those associated with aerodynamic performance. It is difficult to quantify these effects from flight experience since they occur usually together with other effects such as wind shear and downdraft. It is known, however, that heavy rain can increase the effective thickness of a wing and cause roughness which stems from drop impingement and from waviness of the liquid film. These effects can, in turn, influence the transition from laminar to turbulent flow and increase drag while decreasing lift. They are significant at all angles of attack and can be important at the higher angles associated with landing configurations. More will be said of this topic later in the course by Dunham.

Knowledge of insect contamination is less, mainly because the likely consequences are small. It is assumed that the contamination acts as distributed roughness with maximum height in the region of the leading edge. The contamination tends to be removed at high speeds or in the presence of rain.

The formation of ice is usually confined to the leading-edge region and again has maximum importance at the high angles of attack associated with landing and takeoff. Deicing is carried out where possible and can avoid or reduce the problem but, as is known from recent accidents, ice can form rapidly on the leading edge of wings and intakes with considerable consequences for aerodynamic properties. Ice formation can also occur at cruise conditions and to an extent that lift is reduced by an important amount. It can be considered in two ways, the first where the effective shape is changed and the second where the ice acts as an equivalent sand-grain roughness although both can be important in many circumstances.

The following section examines the experimental evidence for the effects of rain, insects and ice on airfoil performance and considers the extent to which the available information can be incorporated in a calculation method in terms of change of shape and surface roughness. It is easy to envisage that a major shape change will have effects which can be described by the same procedures which led to the arrangement of the original airfoil. In a similar manner, roughness can be incorporated in the solution of boundary-layer or the Navier-Stokes equations provided the characteristics of the roughness are known. Thus the experimental knowledge of rain, insects and ice must be presented in the form of equivalent roughness. It is also known that the environmental effects can affect the onset of transition and, since this can be important with low Reynolds-number airfoils and with attempts to ensure laminar-flow airfoils, this evidence is also examined.

The experimental information has been used traditionally in the form of correlation equations and these are reviewed in Section 3. The advantage of these correlations is that they can provide accurate representation within the limited range of the data but they are restricted by their lack of a physical basis for the equation.

The fourth section of the paper considers the components of a method, based on more fundamental equations, to calculate the performance of airfoils as a function of shape, angle of attack and Reynolds number. One procedure is described in greater detail and the ways of accommodating changes to the airfoil shape and surface roughness are considered. It involves the numerical solution of conservation equations in differential form and has been used to obtain results which are presented in Section 5 and allow appraisal of the numerical features of the calculation method and of the extent to which it can predict the known environmental effects.

2.0 Experimental Evidence

The effects of rain have been examined in the wind-tunnel tests of Reference 1 and more recently in References 2 and 3. The magnitude of the rain falls considered stem from arguments similar to those of Haines and Luers [4] who examined the records of the U.S. weather stations and concluded that the yearly mean-maximum rainfall rate over a 60 sec period in the

eastern United States ranged from 150 to 250 mm/h. It is expected that shorter term averages will achieve larger values and it should be noted that the record rainfall rate is 1830 mm/h. Although these torrential rainfalls are uncommon, it is desirable to know their likely consequences.

The average thickness of the film of water on a 10m chord airfoil and fuselage at zero angle of attack was calculated in Reference 4 and is shown on Table 1. It is unlikely that the distribution of film thickness would be uniform and increasing angle of attack is likely to lead to increased thickness in the trailing-edge region since the drag force between the air and water will decrease from around midchord. Thus, the trailing-edge region can be expected to support film thicknesses considerably greater than those of Table 1, so that the effective shape of the airfoil can be altered by the rain to imply an adverse pressure gradient in the aft part of the upper side of the airfoil which is reduced by an additional displacement of, say, 3 mm. This will have little importance to lift at cruise but can be more important at high angles of attack.

The raindrops fall on an established film and cause an effective roughness as does the existence of waviness in the downstream flow. So far, all theoretical attempts have made use of an equivalent sand-grain roughness and Table 2, taken from Ref. 4, shows the sand grain roughness equivalent for a range of rainfall. The corresponding increase in skin-friction drag is shown on Table 3 and is appreciable, although unlikely to be important in terms of fuel consumption for the assumed limited period of the heavy rainfall. The variations in maximum lift coefficient and stall angle associated with the two forms of roughness are shown in Table 4. Taken together with the expected modified airfoil shape, the effects of the rainfall are clearly important at high angles of attack.

The experimental evidence of the effect of rain on airfoil performance is meager and sometimes contradictory. For example, the tests of Ref. 2 on an NACA 64-210 airfoil at $R_c = 2.6 \times 10^6$ with slat and flaps extended showed that a lift loss of up to 30% was possible but results with the same configuration at $R_c = 1.8 \times 10^6$ showed a much smaller lift loss. The reason for this difference is not known but the possibility of the runback water clogging the flap gaps had been mentioned as a possibility. It has

Table 1. Average film thickness for a symmetric airfoil and fuselage at 0-deg angle of attack, 10-m chord

Rainfall rate, mm/h	Calculated thickness airfoil, mm	Estimated thickness fuselage mm
100	≤0.2	≤0.2
200	0.5 or less	0.2 or less
500	0.8	0.6
1000	1.0	0.9
2000	1.3	1.1

Table 2. Equivalent sand-grain roughnesses by rainfall rate on a wing

Rain rate mm/h	k_s, mm	
	Drop Impact Cratering	Waviness
100	0.18	<0.3
200	0.37	0.7
500	0.89	1.2
1000	1.83	1.5
2000	3.65	2.0

Table 3. Increase in total drag due to increased wing and fuselage friction drag (747 aircraft landing configuration)

Rainfall rate	$\Delta C_D/C_{D_0}$, %	
	Drop Impact Cratering	Waviness
100	1.6	2.1
200	2.3	3.2
500	3.5	3.8
1000	4.6	4.2
2000	5.9	4.6

Table 4. Reduction in maximum lift coefficient and angle of attack at stall due to roughness

Rain rate, mm/h	$\Delta C_L/C_L$, %		$\Delta\alpha_{C_{L_{max}}}$, deg	
	Drop impact cratering	Film waviness	Drop impact cratering	Film waviness
100	7	11	1-2	1-3
200	13	20	1-3	2-4
500	25	25	2-5	2-5
1000	29	28	3-5	3-5
2000	34	30	3-6	3-5

also been pointed out that wind tunnel experiments simulating flight in rain should be properly scaled in order to model full-scale conditions and that this involves careful consideration of the transition process and of wind-tunnel characteristics. The added influence of the type of surface has been demonstrated in Reference 3 for a low Reynolds-number airfoil (Wortmann FX-67-K-170) with the resulting lift and drag coefficients of Figure 1. In these experiments, the equivalent rainfall was 440 mm/h and the chord Reynolds number 310,000. It is evident from the figure that the maximum lift and minimum drag are obtained with a dry surface and that the combination of simulated rain and a range of surface coatings is to reduce lift and increase drag. The surface with a clean epoxy gel may be regarded as closest to that of a commercial aircraft but the addition of wetting agents is relevant to surfaces which have been deiced or washed with detergent. It is particularly important to observe the magnitude of the decrease in lift, which occurs close to the angle of attack corresponding to maximum lift.

The effects of Figure 1 are, in some measure, particular to the low Reynolds number of the investigation so that it may be that the location of transition has been moved forward by the simulated rain. Experiments were performed with three different positions of a boundary-layer trip and led to the results of Figure 2, which shows that effects of similar magnitude to those of Figure 1 can be achieved in the absence of the simulated rain by tripping the boundary layer at locations up to midchord. The trip was a 2mm-wide strip of sand grains of 0.3mm average size so

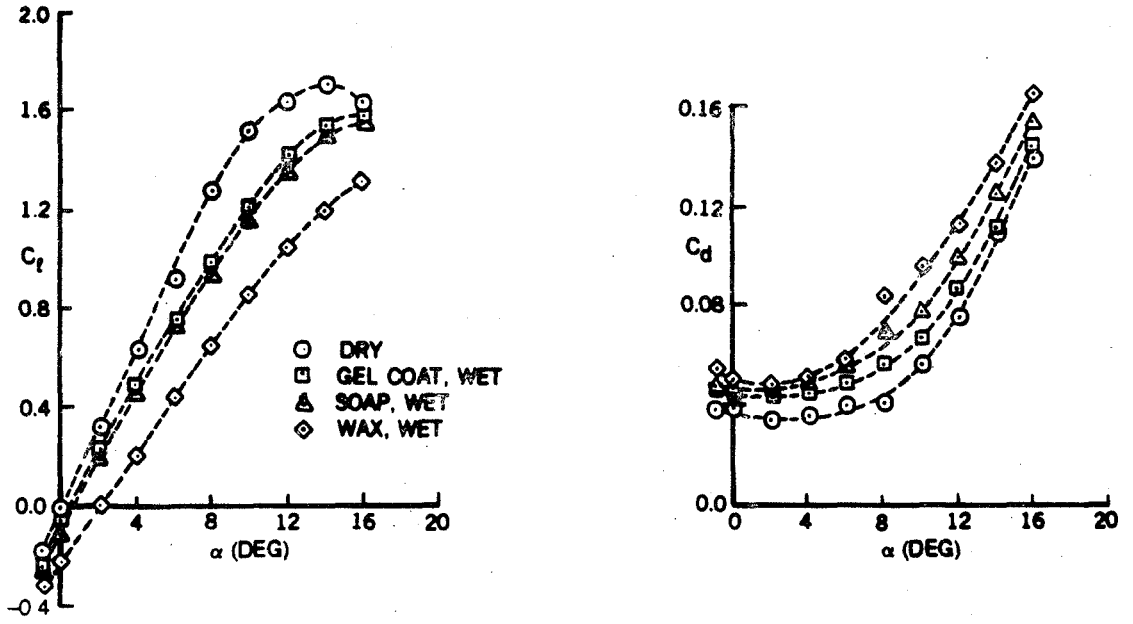

Fig. 1. Effect of surface conditions on lift and drag coefficient as a function of angle of attack (Ref. 3).

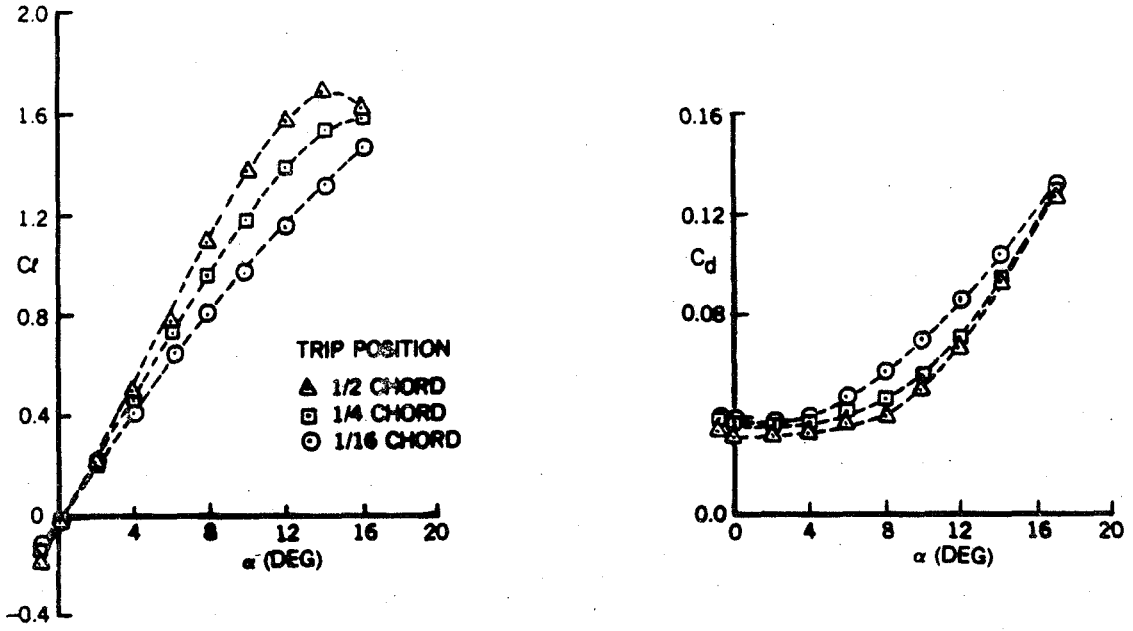

Fig. 2. Effect of boundary layer trip on the lift and drag coefficients as a function of angle of attack (Ref. 3).

that, as can be seen from Table 2, it is similar to the equivalent sand-grain roughness of the simulated rain. The position of transition on the wings of commercial aircraft is usually close to the leading edge, so that the nature of the surface is less important but the differences between the dry results and those obtained with simulated rain and the gel coat, Figure 1, indicate the likely effect of heavy rain. In addition, novel

designs involving procedures to maintain laminar flow must take account of the implications of Figures 1 and 2.

Experimentally based information of the effects of insect contamination is less than that for rain or ice, is confined to low speeds and has been considered mainly in relation to the location of transition. This is an important aspect of laminar control since insect contamination first appears near the leading edge so that laminar flow can be lost if a critical level is exceeded. It has been found that insect contamination acts as distributed roughness and in this sense it may be treated by computational methods once the statistical properties of insects are known. Experiments indicate that, for contamination to occur, a minimum speed, probably different for different species, has to be exceeded so that the insects burst on impact and adhere to the surface. Impact regions or capture areas can be calculated by computer programs used for water-droplet trajectory and impingement calculation by substituting for insect mass and drag coefficient. Experiments made on 5-foot-chord airfoils at $R_c \sim 7 \times 10^6$ with fruit flies showed maximum roughness heights in the range of 0.015 - 0.030 inches can occur near the stagnation point (Ref. 5). It was found that the roughness height decreased rapidly with distance from the leading edge and the effect of this local buildup on the airfoil performance was small. The experiments were, however, restricted to low angles of attack and larger effects can be expected at large angles because the area of peak velocity may occur not far from that of insect impact. Quantification of this hypothesis can be obtained with the calculation method of Section 4. Although no direct tests of insect contamination effect on maximum lift are available, it can be assumed that it would be similar to that of a distributed roughness.

It is evident from Refs. 6 to 10, that ice accretion may affect the aerodynamic characteristics of airfoils by reducing $C_{\ell\ max}$ and increasing drag. Two types of ice may form, rime ice where low temperatures and velocities allow supercooled water droplets to freeze on impact with a resulting accretion similar to that of Figure 3a and glaze ice at temperatures just below freezing so that water droplets flow along the surface and freeze to glaze-ice forms similar to those of Figure 3b. Both types of ice can influence lift and drag considerably by the modified shape of

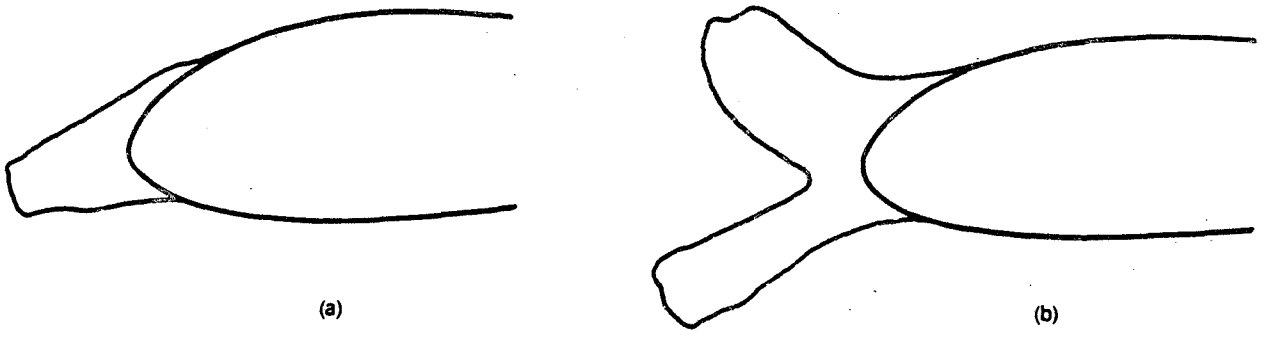

Fig. 3. Typical (a) rime and (b) glaze ice accretions on the leading-edge of an airfoil.

the effective airfoil; they also contribute to added drag, and reduced lift, through surface roughness.

The influence of ice accretion on the aerodynamic properties of airfoils has been investigated experimentally over many years. In the 1950's, the NACA investigated the effects of ice on airfoil performance and some of these results can be found in the work of Gray and Von Glahn [6] who examined NACA 65-212 and 65A004 airfoils and showed the adverse effects of ice on the integrated lift, drag and moment. Other investigations, such as that by Korkan et al. [7], quantified the effects of simulated ice shapes on airfoil performance and, more recently, Bragg and Coirier [9] simulated a measured glaze ice accretion on a wooden 21-inch chord NACA 0012 airfoil and reported measurements of surface pressures, lift and moment coefficients and a wake survey to provide airfoil drag. The separation bubble was explored by measuring the time-averaged velocities using a split-film probe and velocity profiles were obtained in the separation bubble for several chordwise stations at three angles of attack. The results show that the ice shape caused a severe reduction in lift and substantial increase in drag.

A comprehensive investigation of the efforts of accretion of frost and various ice formations has been reported by Roed [10] who presents variations in lift coefficient measured with a single airfoil, with a trailing flap and with extended slat and flap. The measurements [11] were obtained in a wind tunnel and show very large modifications of the curve of lift

against angle of attack, particularly with the trailing edge extended. The angle of attack corresponding to $C_{L\ max}$ can be changed from 9 to 1 degree with corresponding reduction in $C_{L\ max}$ from 3.5 to 2.8. With the multi-element configuration, corresponding reductions in $C_{L\ max}$ from 4.3 to 3.3 were observed.

It is evident that the main effect of ice accretion is to change the shape of the airfoil and so modify its performance. The prediction of the flow characteristics which result from the accretions can be achieved by the solution of inviscid and viscous-flow equations and interaction of the solutions or of the Navier-Stokes equations. As has been shown in various papers, for example Reference 12, interaction between the inviscid and viscous flow equations becomes increasingly necessary as the angle of attack is increased. In addition, it is desirable to make provision for the roughness of the ice surface in a general manner which will also accommodate the related roughness effects of rain and insect contamination. To provide this generality, and to permit the inclusion of accretion model, an interactive boundary-layer procedure, based on the solution of differential equations in finite-difference form is advocated and a preferred approach is described in Section 4.

3.0 Data Correlations

Roughness caused by rain, frost, snow or freezing fog adhering to the wing surface, large accumulations of insect debris and badly chipped paint can play an important role on aircraft flight performance. These adverse effects are addressed in the Federal Air Regulations and have received considerable attention in the past several years. Due to the immense complexity of the problem, however, estimation of the roughness effects are presently limited to data correlations. Computational methods which offer broader applicability, accuracy an fundamental understanding are very new, as discussed by Shaw [13,14] and their development has so far been limited to airfoils. Before we discuss these recent and advanced computational methods for airfoils and their possible extension to wings, empennage, propellers, rotors and eventually for complete aircraft configurations, it is useful to review the correlations which provide insight into the effects of small amounts of wing-surface roughness on aircraft flight performance. In addition, the shortcomings of correlations for predicting the effects

of ice on lift and drag of airfoils are considered. Previous reviews of performance degradation of propellers, helicopter rotors (hover and forward flight) and complete aircraft are available in References 14 to 20.

As discussed by Brumby [21] for full wing-span upper surface roughness beginning at the leading edge and extending varying distances aft, typical effects are a reduction of the maximum lift coefficient (increase in stall speed), a reduction in the angle of attack at which stall occurs and a rapid post-stall drag increase (see Fig. 4). The effects become more severe as the size and chordwise extent of the roughness increase and they may be accompanied by a reduction in lift at a given angle of attack and by an increase in the parasite drag.

Figure 5 shows Brumby's correlation of wind tunnel and flight data and the effects of surface roughness on the maximum lift coefficient of a wing. The majority of the data are from two-dimensional tests but the four flagged points represent data obtained from three-dimensional swept surfaces and appear to confirm that the correlation is applicable to wings. The data are for two general types of roughness on wings without leading-edge high-lift devices. The solid symbols indicate data for distributed (sand-grain type) roughness at the leading edge, or on the entire upper surface, and the open symbols correspond to localized full-span

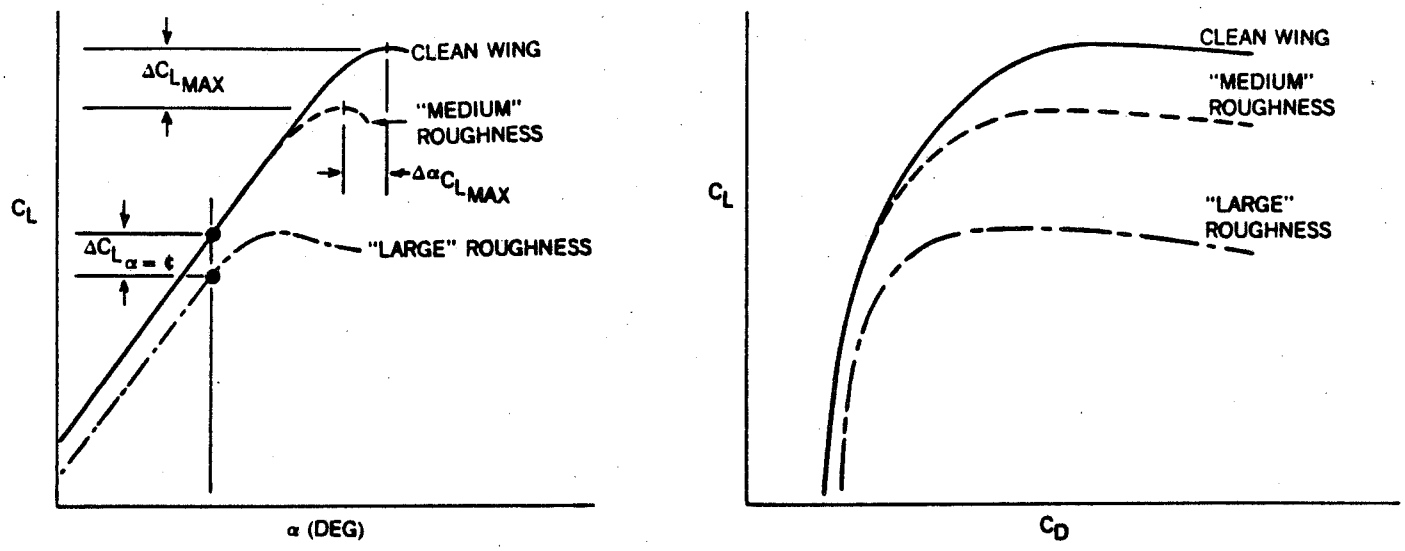

Fig. 4. Typical effect of surface roughness at the leading edgeon aerodynamic characteristics.

ORIGINAL PAGE IS
OF POOR QUALITY

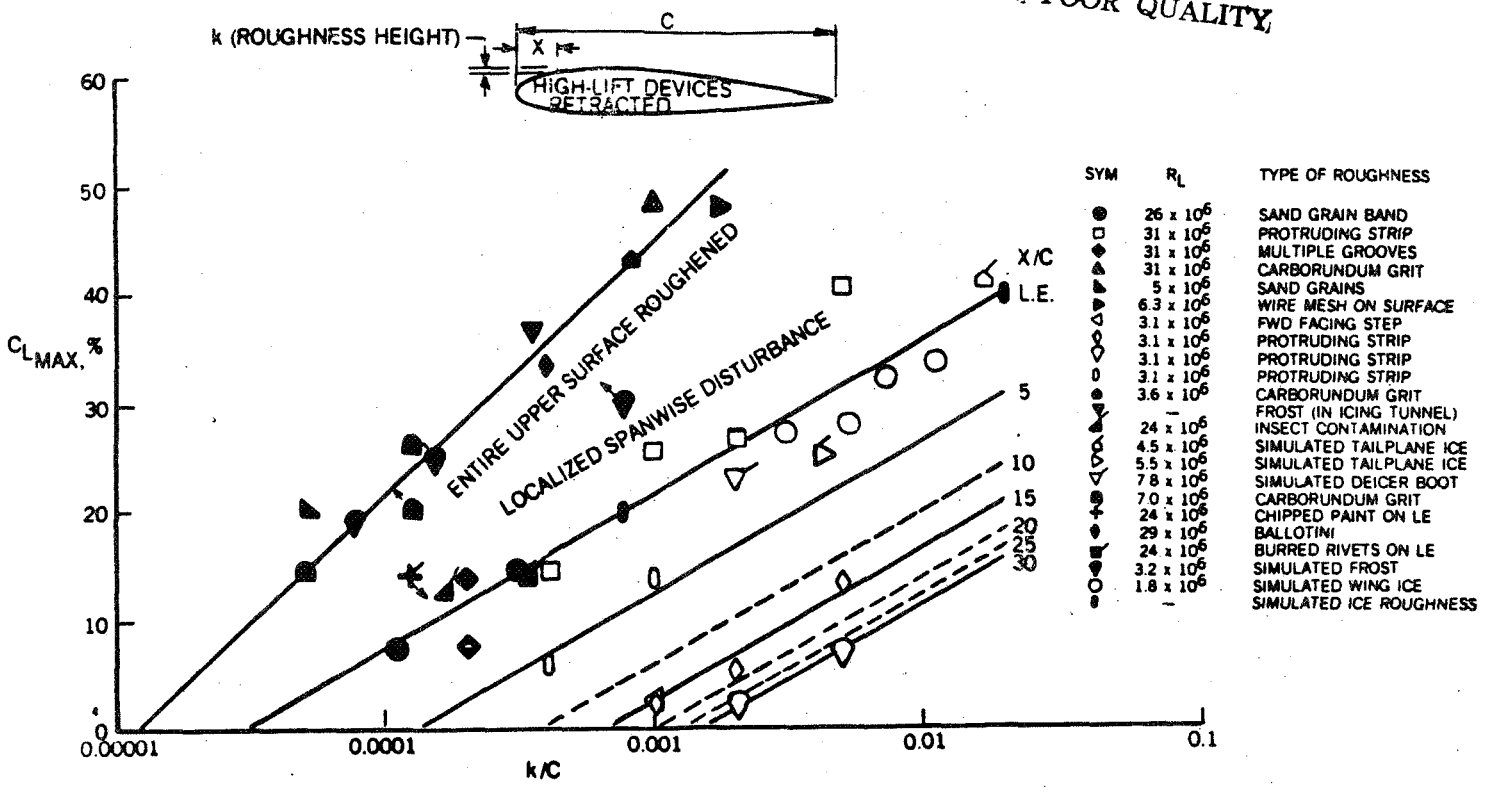

Fig. 5. Reduction of maximum lift coefficient due to wing surface roughness.

disturbances at various chordwise stations. It is clear that large decreases in $C_{L\ max}$, with resultant large increases in stall speed, can occur due to comparatively minor wing surface disturbances.

Bragg et al. [20] claim that Brumby's correlation, while useful in estimation of changes in $C_{L\ max}$, is limited in that it contains no Reynolds number effects and little detail of the actual roughness or its density. As a consequence, it fails to predict the measured results of increased $C_{L\ max}$ due to ice accretions.

An early correlation equation for the effects of ice on drag was formulated by Gray [22] and based on the data collected in the NASA Lewis Icing Research Tunnel (IRT) primarily in the 1950's. It is best suited for glaze conditions and Fig. 6, taken from Ref. 14, shows that it provides guidance, though the predicted drag rise is often too large. More recently, Bragg [23] developed a rime-ice correlation, also based on the data gathered in the NACA IRT. Flemming [18] acquired a large data base in the Canadian

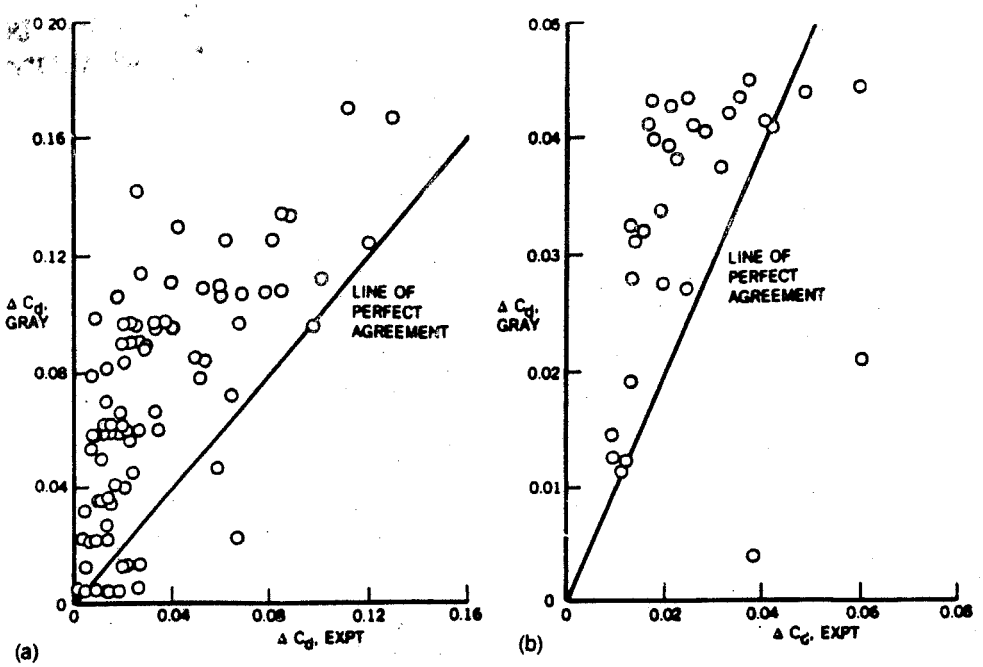

Fig. 6. Gray's drag rise correlation for two airfoils: (a) NACA 0012 (b) NASA MS(1)-0317, both taken from Ref. 14.

NRC high-speed icing wind tunnel for a series of reduced scale rotor airfoil sections which he used to develop a series of correlations for the drag rise due to ice accretions. Figure 7 shows Flemming's correlation for the same two airfoils as Fig. 6, also taken from Ref. 14 and that contrary to Gray's correlation, it provides a lower drag rise.

It is evident from the results discussed above and from the additional examples of Ref. 14, that the experimental data involve effects not represented by the correlation equations. They are confined mainly to drag and do not include terms to take account of known effects such as those of Reynolds number, airfoil shape and slats. There is a clear need for a procedure which will represent the aerodynamic properties of the flow around airfoils correctly and will allow correct representation of large changes in geometry, such as those associated with accretions of rime and glaze ice, as well as the smaller changes associated with frost, insects and rain. It is also desirable that this procedure should be able to deal with the three-dimensional effects of real airplanes. The following section addresses these needs.

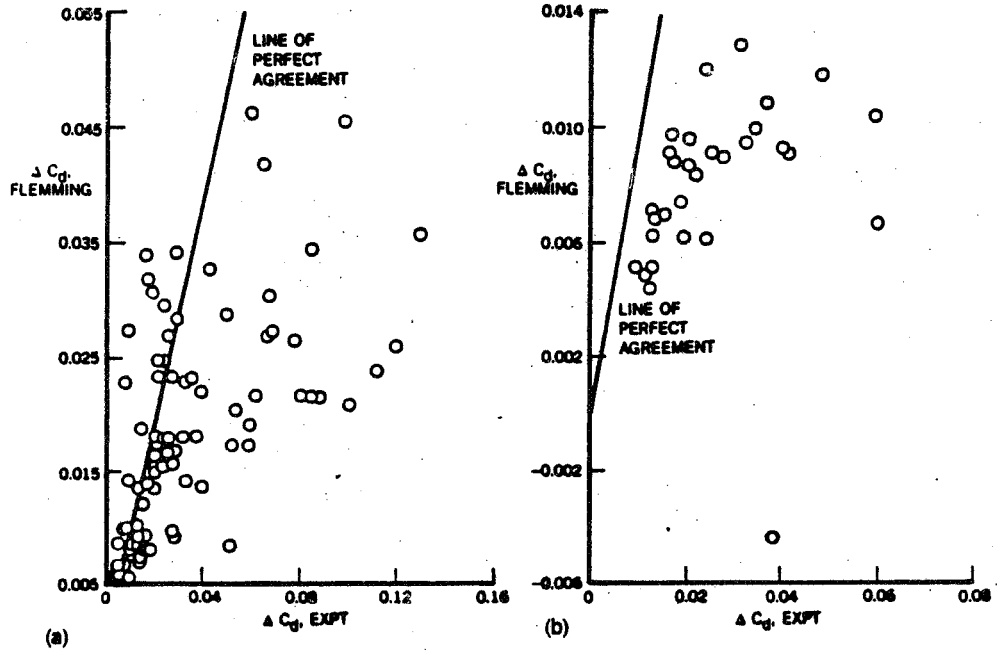

Fig. 7. Flemming's drag rise correlation for two airfoils: (a) NACA 0012 (b) NASA MS(1)-0317, both taken from Ref. 14.

4.0 Numerical Solution Procedures

The development of digital computers, and their ability to solve many algebraic equations in a short time, has spawned considerable efforts to solve the conservation equations of fluid mechanics and heat transfer in differential form. In the field of aerodynamics, these numerical solution procedures have been directed to the solution of reduced forms of the Navier-Stokes equations and particularly to interactive boundary-layer and thin-layer Navier-Stokes equations. Reviews, such as that of Cebeci and Whitelaw [25] show that useful calculations can already be performed for two- and three-dimensional flows and over an extensive range of angle of attack.

Two approaches have been used to obtain the results of Section 5, and are based on the interactive boundary-layer procedure of Cebeci et al. [12] and on the thin-layer Navier-Stokes procedure developed at NASA Ames [26, 27]. The following paragraphs provide outlines of these two approaches and Subsection 4.1 a more detailed description of the interactive procedure, which has been used to obtain most of the results of Section 5. The turbulence

model and the modifications necessary to deal with rough surfaces are considered in Subsection 4.2.

The interactive procedure involves solution of inviscid-flow equations and of boundary-layer equations. The results of Section 5 were obtained with steady, two-dimensional equations. The inviscid flow was determined by conformal mapping and by a panel method and the boundary-layer equations, with turbulent diffusion represented by an eddy-viscosity approach, were solved by the two-point finite-difference method of Keller. Interaction between the inviscid and viscous flows was achieved by a blowing-velocity distribution which was linked to the displacement-thickness distribution through the Hilbert integral. Where separation was encountered, the equations were solved in inverse form with the FLARE approximation which neglects longitudinal convection in the recirculation region. The same approach was taken in the wake where the dividing streamline was computed from the inviscid flow as a line having constant stream function and was used by the inviscid method to apply the blowing velocity required to simulate the displacement thickness and to compute the inviscid velocity. An inviscid point distribution in the wake was defined on which the wake velocity distribution was determined. This required interpolation of the boundary-layer blowing velocity onto the inviscid points. In addition, the computed inviscid velocity was interpolated back to the boundary-layer points by making use of the computed velocity at the trailing edge as the initial wake point. In the immediate vicinity of the trailing edge, particular care was required in the choice of the locations at which values of the blowing velocities were applied in the solution of the inviscid equations. Further details are provided in the following subsection.

The thin-layer Navier-Stokes equations are generally referred to in the literature as TLNS equations and are obtained by neglecting streamwise and spanwise derivatives of the viscous and turbulence stress, conductive heat-flux terms, and any term involving mixed derivatives. These approximations are justified either by order of magnitude arguments or by consideration of computational accuracy argument [28,29]. The TLNS equations have been proposed mainly on the computational argument. The form of the equations generally used does not satisfy relationships between metric coefficients in diffusive and conduction terms but the resulting error is usually insignificant, except when the effective viscosity is relatively large.

In addition, longitudinal-curvature diffusive terms are neglected as a consequence of the Cartesian velocity components.

An implicit numerical method was used to solve the TLNS equations and is based on that of Ref. 30. Since only steady-state computations are of interest, a diagonal form for the Euler equations and a spatially varying time step were used. Reference 27 provides a description of the numerical scheme to obtain the results presented here. The turbulence model incorporated in the code is described in Ref. 31.

4.1 Interactive Boundary-Layer Procedure

The outline of the interactive approach provided above is expanded in this section so as to allow more detailed assessment of its features. The conformal-mapping method for the solution of the inviscid-flow equations has been described extensively in the paper by Halsey [32] and the panel method by Hess and Smith [33] to which the reader is referred for further information.

The boundary-layer equations are solved in their two-dimensional form,

$$\frac{\partial u}{\partial x} + \frac{\partial v}{\partial y} = 0 \tag{1}$$

$$u \frac{\partial u}{\partial x} + v \frac{\partial u}{\partial y} = u_e \frac{du_e}{dx} + \nu \frac{\partial}{\partial y} \left(b \frac{\partial u}{\partial y} \right) \tag{2}$$

where $b = 1 + \varepsilon_m/\nu$ and ε_m is defined by a form of the eddy-viscosity formulation of Cebeci and Smith [34] discussed in Subsection 4.2. For wall boundary-layer flows, the boundary condition may be written as

$$y = 0, \quad u = 0, \quad v = 0; \qquad y \to \delta, \quad u \to u_e \tag{3}$$

and for the asymmetric wakes of airfoils,

$$y \to -\delta_\ell, \quad u = u_e, \qquad y = y^*, \quad v = 0, \quad y \to \delta_u, \quad u = u_e \tag{4}$$

Here δ_ℓ and δ_u denote the lower and upper wake boundary-layer thicknesses, respectively, with y^* representing the dividing streamline assumed to be given. The above equations assume that there is no pressure gradient across the shear layer but the corresponding constraint can be removed for strongly curved wakes.

The solution of Eqs. (1) and (2) can also be obtained by a procedure in which the external velocity is computed as part of the solution. This procedure is known as the inverse problem and is essential to remove the singularity associated with an external boundary condition based on a specified distribution of u_e. It is necessary to specify an additional boundary condition in addition to the boundary conditions given by Eqs. (3) and (4) since $u_e(x)$ now represents an unknown and, in the interactive scheme of Cebeci et al. [12], this is accomplished by rewriting the external velocity, $u_e(x)$ as

$$u_e(x) = u_e^o(x) + \delta u_e(x) \tag{5}$$

where $u_e^o(x)$ denotes the inviscid velocity and $\delta u_e(x)$ is the perturbation velocity due to viscous effects. The latter is related to the blowing velocity induced by the boundary layer by a variation of the Hilbert integral

$$\delta u_e(x) = \frac{1}{\pi} \int_{x_a}^{x_b} \frac{d}{ds}(u_e \delta^*) \frac{d\sigma}{s - \sigma} \tag{6}$$

with the interaction region limited to a finite range $x_a \leq x \leq x_b$.

Following Cebeci and Clark [35], we write Eqs. (5) and (6) as

$$u_e(x) = u_e^o(x) + \sum_{j=1}^{n} c_{ij}(u_e \delta^*)_j \tag{7a}$$

Here c_{ij} denotes the interaction-coefficient matrix, which is obtained from a discrete approximation to the Hilbert integral in Eq. (6). In this form, Eq. (7a) represents an outer boundary condition for the inverse problem. It can be generalized to the form

$$u_e(x) = u_e^k(x) + \sum_{j=1}^{n} c_{ij}[(u_e \delta^*)_j - (u_e \delta^*)_j^k], \tag{7b}$$

where $u_e^k(x)$ corresponds to the inviscid velocity distribution which contains the displacement effect $(\delta^*)^k$ computed from a previous sweep.

The solution of Eqs. (1) and (2) for the inverse problem is now obtained subject to Eqs. (3) for wall boundary layers and to Eqs. (4) for wake flows with $u_e(x)$ given by Eq. (5). It is convenient to express the above

equations in terms of transformed coordinates and, with u_o denoting a constant reference velocity, we introduce the transformation

$$\eta = \left(\frac{u_o}{\nu x}\right)^{1/2} y, \qquad \psi = (u_o \nu x)^{1/2} f(x,\eta) \tag{8}$$

With primes denoting differentiation with respect to η, Eqs. (1) and (2) and their boundary conditions on the airfoil and in the wake can be written in the following form:

$$(bf'')' + \frac{1}{2} ff'' + xw \frac{dw}{dx} = x\left(f' \frac{\partial f'}{\partial x} - f'' \frac{\partial f}{\partial x}\right) \tag{8}$$

On the airfoil

$$\eta = 0, \qquad f = f' = 0 \tag{9a}$$

$$\eta = \eta_e, \qquad f' = w, \qquad w - \tilde{c}_{ii}(\eta_e w - f) = g_i \tag{9b}$$

In the wake

$$\eta = -\eta_\ell \qquad f' = w; \qquad \eta = \eta^*, \qquad f = 0 \tag{10a}$$

$$\eta = \eta_u, \qquad f' = w, \qquad w - \tilde{c}_{ii}[w(\eta_u - \eta_\ell) - (f_u - f_\ell)] = g_i \tag{10b}$$

where

$$\tilde{c}_{ii} = c_{ii} \left(\frac{\nu x}{u_o}\right)^{1/2}$$

Here w denotes the dimensionless external velocity u_e/u_o and the parameter g_i, which results from the discrete approximation to the Hilbert integral Eq. (6), is given by

$$g_i = w^k + \sum_{j=1}^{i-1} c_{ij}(D_j - D_j^k) - c_{ii} D_i^k \tag{11}$$

where

$$D = \left(\frac{\nu x}{u_o}\right)^{1/2} (\eta_e w - f_e) \tag{12}$$

The expression for g_i on the wake is nearly identical to that for the airfoil, Eq. (11), except that now Eq. (12) is given by

$$D = \left(\frac{\nu x}{u_o}\right)^{1/2} [w(\eta_u - \eta_\ell) - (f_u - f_\ell)] \tag{13}$$

The numerical solution of Eq. (8) subject to the boundary conditions given by Eqs. (9) and (10) has been obtained with Keller's Box method which is an efficient, second-order finite-difference method extensively used by

Cebeci and his associates for a wide range of flows, as discussed in [36]. The procedure for wake flows is novel and has some desirable features which allow the calculation of thick separated boundary layers by the extension of the interactive scheme. As in the solution of wall boundary-layer flows, we assume

$$f' = u \tag{14a}$$

$$u' = v \tag{14b}$$

and write Eq. (8) as a first-order system

$$(bv)' + \frac{1}{2} fv + xw \frac{dw}{dx} = x(u \frac{\partial u}{\partial x} - v \frac{\partial f}{\partial x}) \tag{14c}$$

The Mechul-function formulation [37] is used to obtain stable solutions to the above equations and to reduce their sensitivity to the boundary conditions which involve f_u and f_ℓ. Since both s and w are functions of w only, we write

$$s' = 0 \tag{14d}$$

$$w' = 0 \tag{14e}$$

and the boundary conditions for the system given by Eq. (14) become

$$\eta = -\eta_\ell, \quad u = w, \quad s = f_\ell; \qquad \eta = \eta^*, \quad f = 0 \tag{15a}$$

$$\eta = \eta_u, \quad u = w, \quad w - \tilde{c}_{11} [w(\eta_u - \eta_\ell) - (f - s)] = g_1 \tag{15b}$$

The system of Eqs. (14) and (15) are solved by the procedure described in Ref. 36. After the finite-difference approximations to Eqs. (14) are written, the resulting nonlinear algebraic system is linearized by Newton's method and the linear system is then solved by the block-elimination method.

In computing airfoil flows with separation [12], again the FLARE approximation was used to obtain stable solutions on the airfoil and in the wake. As the extent of the separation region increased, however, Cebeci et al. [12] introduced an additional iterative scheme based on a continuation method at the start of the wake calculations. With u_{ref} corresponding to a nonseparating velocity profile constructed somewhat arbitrarily from the separated velocity profile at the trailing edge an initial velocity profile was defined by

$$u = u_{ref} + n(u - u_{ref}) \qquad n = 0,\ 0.50,\ 1.0 \quad . \tag{16}$$

and the boundary-layer solution was computed at the first point on the wake with n = 0. The solution was repeated for other values of n until convergence. The procedure was applied for each profile in the wake with separation and was necessary at higher angles of attack near stall conditions. For additional details, see Choi [38].

4.2 Eddy-Viscosity Formulation

The presence of ν_t in b requires a turbulence model and in Ref. 12, the algebraic eddy-viscosity formulation of Cebeci and Smith [34] was used for "clean" airfoils. According to this formulation for wall boundary-layer flows, ν_t is defined by two separate formulas, given by

$$\nu_t = \begin{cases} L^2 \left|\frac{\partial u}{\partial y}\right| \gamma_{tr} & 0 \le y \le y_c \qquad (17a) \\ \alpha \left| \int_0^\infty (u_e - u)dy \right| \gamma_{tr}\gamma & y_c \le y \le \delta \qquad (17b) \end{cases}$$

where with $\kappa = 0.4$

$$\begin{aligned} L &= \kappa y\,[1 - \exp(-y/A)] \\ A &= 26\nu u_\tau^{-1}, \qquad u_\tau = \left(\frac{\tau_\ell}{\rho}\right)^{1/2}_{max}, \\ \tau_\ell &= \mu \frac{\partial u}{\partial y}, \qquad \gamma = \frac{1}{1 + 5.5(y/\delta)^6} \end{aligned} \tag{18}$$

The condition used to define y_c is the continuity of the eddy viscosity; from the wall outward Eq. (17a) is applied until its value is equal to the one given by Eq. (17b). In Eq. (17), γ_{tr} is an intermittency factor which accounts for the transitional region between a laminar and turbulent flow and is given by

$$\gamma_{tr} = 1 - \exp\left[-G(x - x_{tr}) \int_{x_{tr}}^{x} \frac{dx}{u_e}\right] \tag{19a}$$

Here G is an empirical parameter which, with x_{tr} denoting the location of the start of transition and $R_{x_{tr}}$ the transition Reynolds number defined by $R_{x_{tr}} = (u_e x/\nu)_{tr}$, is given by

$$G = \frac{1}{1200} \frac{u_e^3}{\nu^2} R_{x_{tr}}^{-1.34} \tag{19b}$$

According to the Cebeci-Smith (CS) model, the parameter α in Eq. (17b) is equal to 0.0168 for values of R_θ greater than 5000, and is given by the expression in [34] for R_θ less than 5000. Studies indicate, however, that in flows with strong pressure gradient, the value of α should also be changed when $R_\theta > 5000$. For this purpose Cebeci et al. use an expression for α to account for strong adverse pressure gradient effects as discussed in Ref. 12.

The above eddy-viscosity formulation of Cebeci and Smith for "clean" airfoils can also be used for "rough" airfoils with small modifications to the inner eddy-viscosity formula of Eq. (17a) only. We use the formulation of Cebeci and Chang [38] for this purpose and rewrite the modified mixing length expression of Eq. (18) as

$$L = \kappa(y + \Delta y)\{1 - \exp[-(y + \Delta y)/A]\} \tag{20}$$

where Δy is a function of an equivalent sand-grain roughness k_s. In terms of dimensionless quantities with $k_s^+ = k_s u_\tau/\nu$, we have

$$\frac{\Delta y u_\tau}{\nu} = \Delta y^+ = \begin{cases} 0.9\ [\sqrt{k_s^+} - k_s^+ \exp\ (-\ k_s^+/6)] & 5 \le k_s^+ \le 70 \\ \\ 0.7\ (k_s^+)^{0.58} & 70 \le k_s^+ \le 2000 \end{cases} \tag{21}$$

5.0 Results and Discussion

The calculated results are presented in three subsections which deal with smooth airfoils, rough airfoils and iced airfoils, respectively. The first subsection is included to quantify the extent to which the two calculation methods can represent airfoil flows as a function of angle of attack and without the added complication of a roughened surface. The rough surfaces of section two allow examination of the value of the concept of equivalent sand-grain roughness within the framework of the turbulence model of the interactive procedure. Similar results can be expected from solution of the thin-layer equations and from the application of both procedures to

problems of iced airfoils were the ice can be considered as roughness. The last section describes results obtained with the two calculation methods for iced airfoils where the ice accretion changes the shape of the leading edge of the airfoil.

5.1 Smooth Airfoils

Figures 8, 9 and 10 present results obtained with the interactive and thin-layer procedures for two airfoils and angles of attack up to around 16 degrees. They are taken from Ref. 39 in which additional results can be obtained.

Measurements of the flow around a NACA 4412 airfoil have been reported in Refs. 40 and 41 and made use of flying hot-wire anemometry at angles of attack up to that of maximum lift. The Reynolds number based on chord

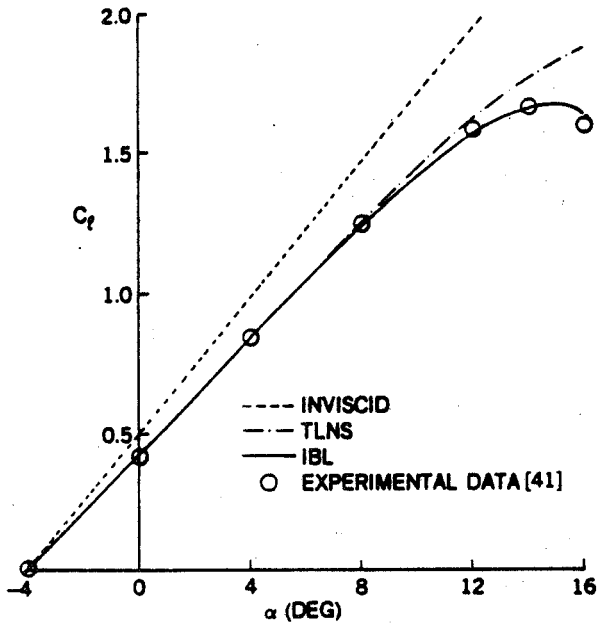

Fig. 8. Variation of lift coefficient with angle of attack for the NACA 4412 airfoil at R_c = 1.523 x 10^6.

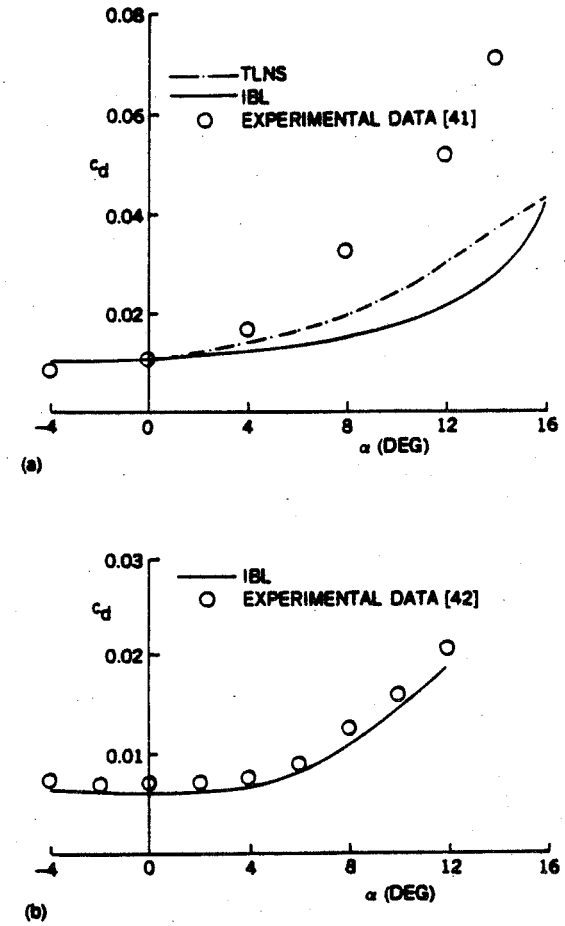

Fig. 9. Variation of total drag coefficient with angle of attack. (a) R_c = 1.523 x 10^6, (b) R_c = 3 x 10^6.

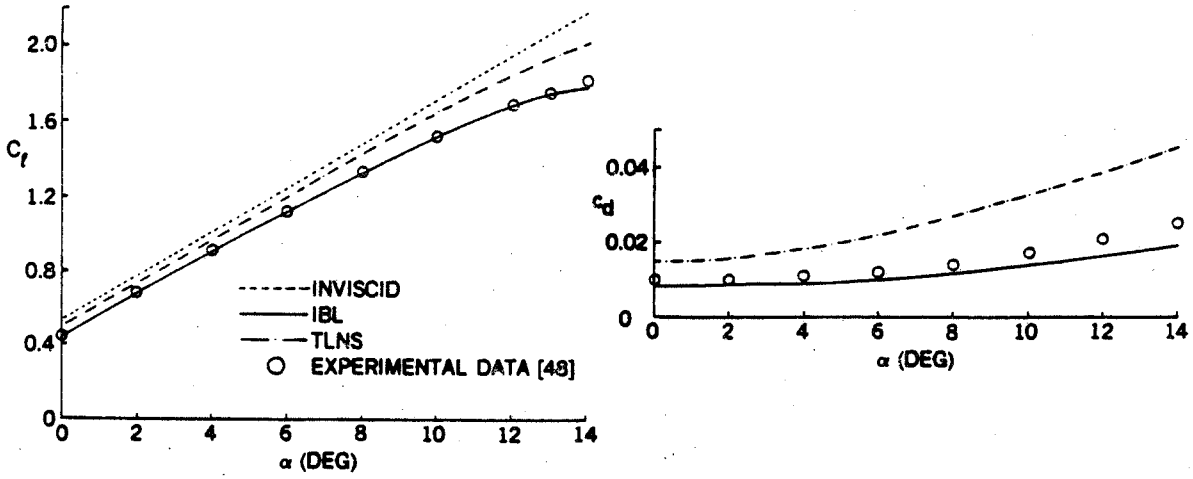

Fig. 10. Variation of lift and drag coefficients for these GA(W)-2 airfoil, $R_c = 4.3 \times 10^6$.

length was 1.523×10^6 and transition was induced at 2.5% chord on the upper surface and 10.3% chord on the lower surface. The same Reynolds number and transition locations were used in the calculations with both methods at angles of attack up to 12 degrees. Above 12 degrees, the interactive calculations revealed a laminar separation very close to the leading edge and the location of the onset of this separation was taken as that of the onset of transition. This assumption is consistent with transition having occurred upstream of the trip in the experiment.

The flow around a NACA 4412 airfoil has also been investigated at a chord Reynolds number of 3×10^6 (Ref. 42) and corresponding calculations have been performed with the onset of transition determined, in the absence of experimental information, by Michel's formula [43] given in Ref. 44, that is

$$R_\theta = 1.174 \left(1 + \frac{22{,}000}{R_x}\right) R_x^{0.46} \qquad (22)$$

or by the onset of laminar separation.

Figures 8 and 9 permit comparison of the measured and calculated values of lift and drag coefficients for the NACA 4412 airfoil. The results for lift coefficient display the variation with angle of attack obtained from the solution of the inviscid-flow equations and which diverges from the measurements with increasing angle. It is clear that the two calculation methods agree well with each other and with experiment up to around 8

degrees beyond which the interaction procedure follows the experimental results more closely and represents the expected maximum value at the same angle of attack on the measurements. This aspect of the comparison of the two calculation methods is similar to that reported in Ref. 31 in relation to a NACA 0012 airfoil, with the two calculation methods agreeing well with each other up to around 14 degrees.

The drag coefficients of Figure 9 are more difficult to appraise since the two experimental distributions differ increasingly with angle of attack and, for example, by a factor of almost two at 12 degrees. Experimental differences are common, due to the inaccuracy of the integrating the wake profile and to wind-tunnel effects associated with blockage or finite span. The magnitude of the present differences is, however, unusual. The results obtained with the two calculation methods agree well with the measurements of Refs. 42 and 45 and are at odds with those of Refs. 40 and 41. They were obtained by wake integration of the interactive boundary-layer results and by surface integration of the TLNS results since, in the latter case, the far wake was not well represented by the calculations.

It is interesting to note that measurements of drag coefficient obtained with NACA 0012 airfoils and described in Refs. 46 and 47 also show discrepancies which increase with angle of attack so that, at 12 degrees, the difference was around 15%. The calculations of Ref. 31 revealed similar discrepancies and it is clear that it is difficult to achieve a high degree of accuracy.

Distributions of pressure coefficients agreed very closely at 0 and 4 degrees angle of attack and agree reasonably well at 12 degrees but with differences in the trailing-edge region and particularly in the representation of the small region of upper-surface separation which affected the wake and led, in part, to better representation of the wake by the interaction boundary-layer method. It was found that the pressure peak was very sharp and located almost at the leading edge. The distributions at 16 degrees revealed an even more peaky pressure distribution and the need to specify the onset of transition upstream of the trip can be appreciated. The discrepancy between the two calculation methods was more evident at 16 degrees and involved a large and important difference in the trailing-edge region where the interactive approach suggested separation some 20% of

chord upstream of the trailing edge and the TLNS method suggested a smaller separation.

The GA(W)-2 airfoil represents a more difficult test since it is a 13% thick airfoil of supercritical form. Measurements have been reported [48] at a chord Reynolds number of 4.3×10^6 and with transition trips at 7.5% chord on both surfaces. Calculations were performed with both methods and, as before, considered the onset of transition in accord with the experimental configuration unless the interactive approach indicated a laminar separation bubble, in which case the onset of transition was taken as coincident with the onset of separation. The results shown in Figure 10 display the variations of lift and drag coefficient with angle of attack.

The deductions which can be made from Figure 10 are similar to those obtained from Figures 8 and 9. The two calculation methods represent an improvement over the inviscid-flow calculations in terms of the lift coefficient and, as before, the interactive method provides results in very close agreement with experiment. The interactive method is also able to calculate the drag coefficient with accuracy which diminishes with angle of attack so that the difference between measurement and calculation is around 20% at 14 degrees. The results of the TLNS method are less satisfactory. A sample of pressure distributions is provided on Figure 11 and, as before, shows the need for proper implementation of the TLNS method in the trailing-edge region.

Before we conclude the discussion on clean airfoils, it is useful to point out the importance of including the wake effect in the interactive boundary-layer method. Studies by Cebeci et al. [12] indicate that in high Reynolds number flows over airfoils at small and moderate angles of attack, it is sufficient to perform the calculations up to the trailing edge. The effect of the wake becomes important at higher angles of attack, especially in flow conditions approaching stall angle, and must be accounted for in the calculations. As can be seen from the results shown in Figure 12a for the NACA 0012 airfoil, the effect of wake on the trailing-edge displacement thickness is negligible for $\alpha = 10°$ but more than 30% for $\alpha = 16°$ indicating that without the wake effect, the magnitude of the trailing-edge displacement thickness is significantly greater than its value with the wake effect. The reduction of the displacement

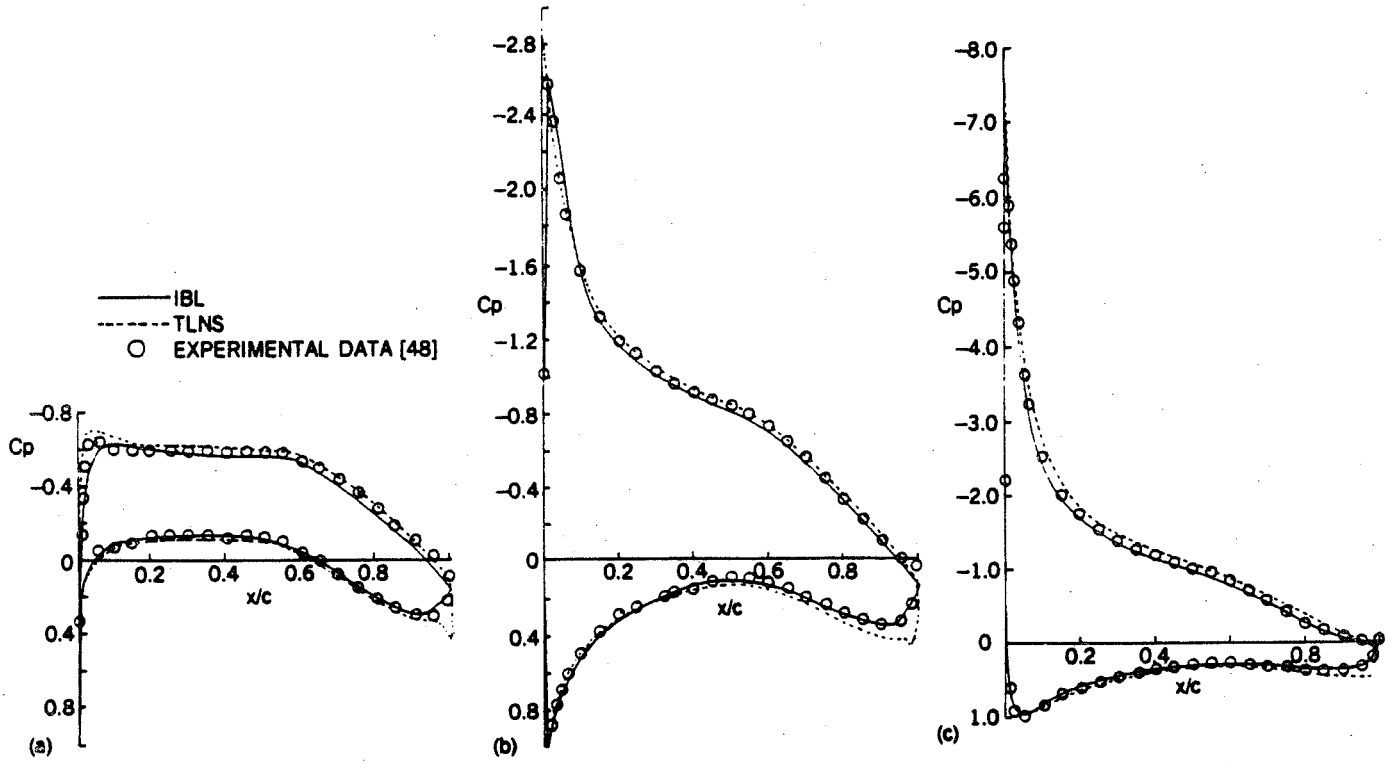

Fig. 11. Comparison of calculated and experimental pressure distributions for the GA(W)-2 airfoil, R_c = 4.3 x 10^6. (a) α = 0°, (b) α = 6°, (c) α = 12°.

thickness reduces the flow separation on the airfoil and decreases the lift coefficient, as shown in Figures 12b and 12c, respectively.

The effect of wake is also important at low Reynolds number flows, which are dominated by large regions of separation bubbles leading to relatively large trailing-edge displacement thicknesses even at low angles of attack. This situation is analogous to high Reynolds number flows over airfoils at high angles of attack and again it requires the inclusion of the wake in the calculations. Further details are provided in Ref. 49.

5.2 Rough Airfoils

To examine the ability to deal with airfoils with rough surfaces, the experiments of [50] were represented by the interactive boundary-layer method. The roughness comprised 0.001 inch carborundum grains applied to 24-inch chord airfoils and spread evenly over a surface length of 0.08 chord. Within the framework of the turbulence model of Subsection 4.2, it is necessary to convert this form of roughness into equivalent sand-grain roughness. This was done with the procedure of Smith and Kaups [51] in

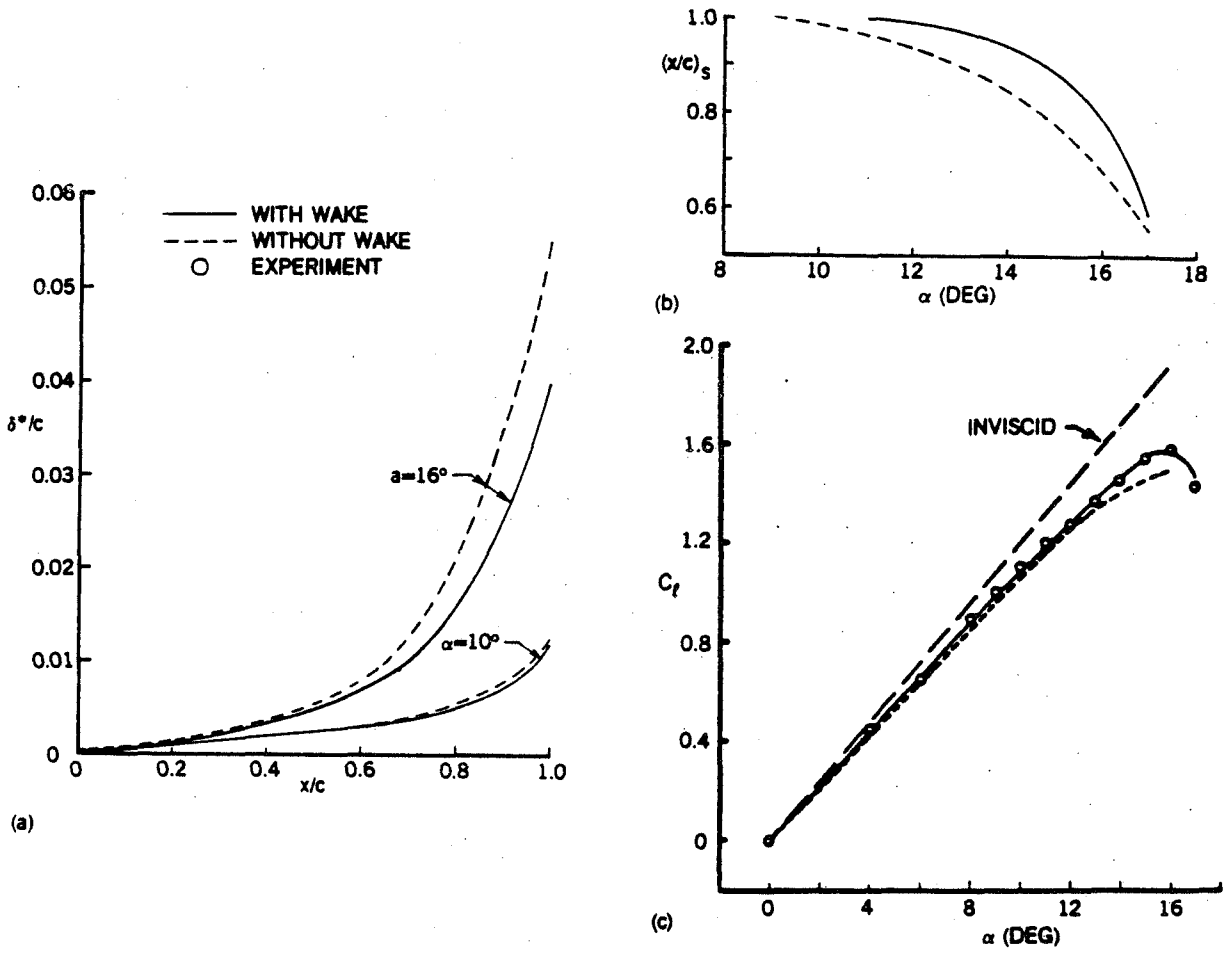

Fig. 12. Effect of wake on the (a) displacement thickness, (b) separation region, and (c) lift coefficient for the NACA 0012 airfoil, $R_c = 6 \times 10^6$.

which the ratio of the equivalent sand-grain roughness to the roughness of the applied elements, k_s/k, was assumed to be a function of the concentration and shape of the roughness elements, see Fig. 13. In all cases considered here, the shape of the elements was approximated by a sphere, and the concentration, which represents the mean value of the area covered by the roughness elements was taken as 0.075 and the equivalent sand-grain roughness height was obtained from Fig. 13 to be

$$k_s/c = 0.00094 \qquad (23)$$

The above expression was used for three airfoils NACA 4412, 23012 and 0012 for which experiments were performed at a Reynolds number of $R_c = 6 \times 10^6$.

Figures 14 and 15 contain the results of the computations for the NACA 4412 airfoil. It can be seen from the lift coefficient results of Fig. 14a that the computations and measurements agree well up to the stall angles for the smooth airfoil as well as for the airfoil with leading-edge roughness. The drag curves of Fig. 14b also show good agreement between computations and measurements although for the clean airfoil the drag is slightly underpredicted at higher angles of attack. Values of dimensionless displacement thickness δ^*/c at the trailing edge are shown in Fig. 15a and, since the transition location is much further

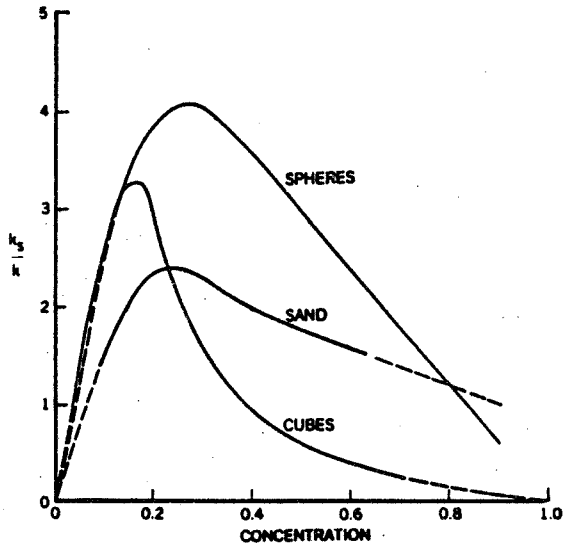

Fig. 13. Equivalent sand-grain roughness for uniform three-dimensional roughness as a function of concentration. Dashed lines are extrapolations of experimental data [51].

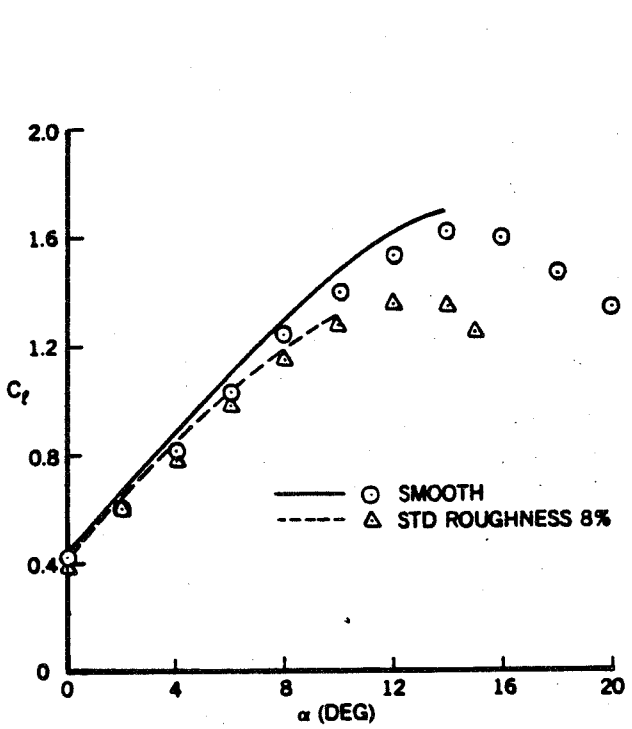

(a)

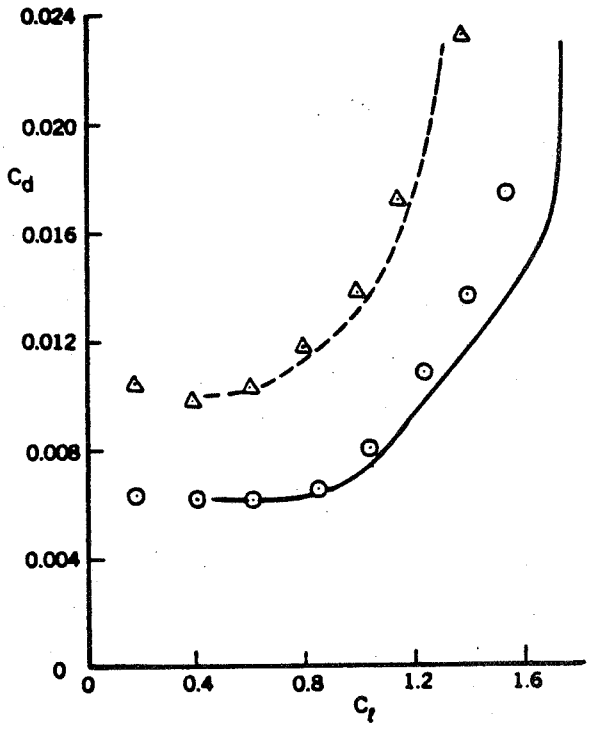

(b)

Fig. 14. Comparison of calculated and experimental results for the NACA 4412 airfoil at $R_c = 6 \times 10^6$.

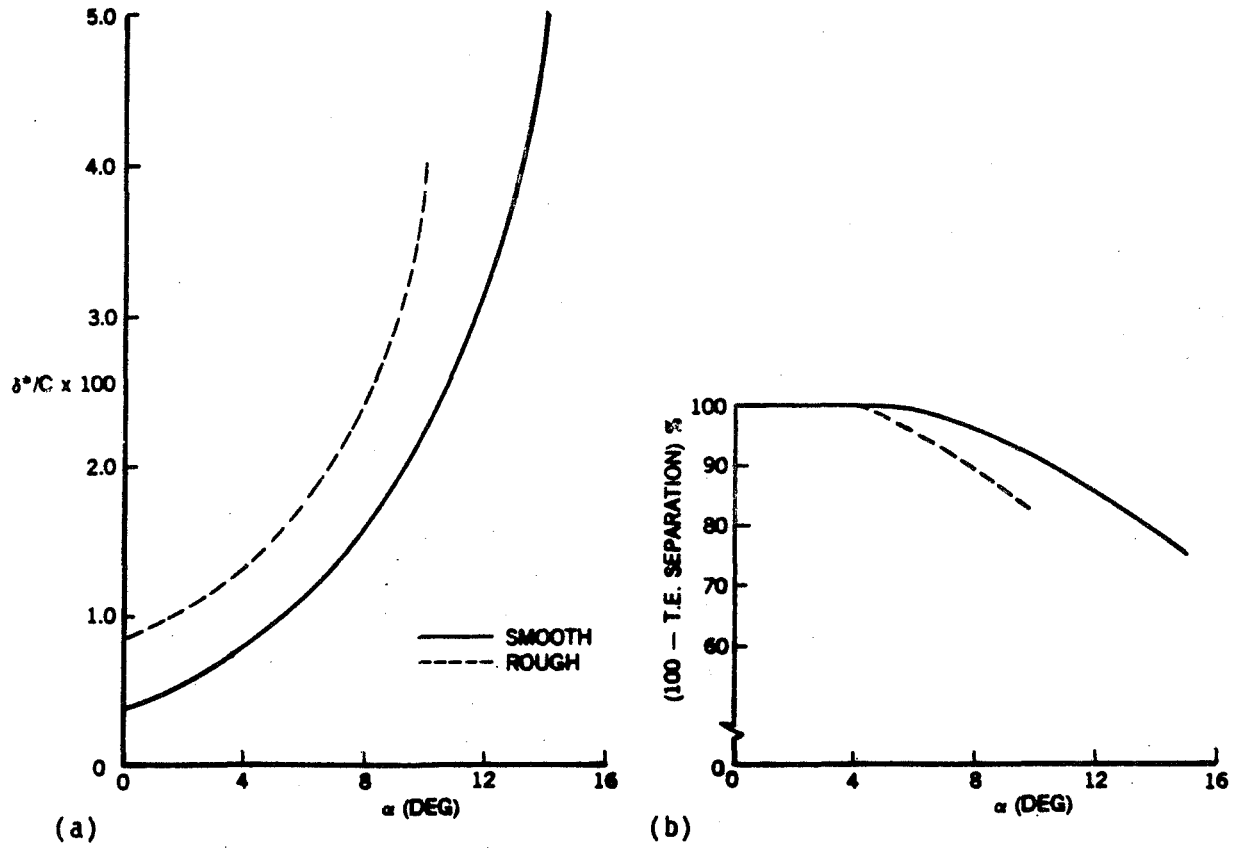

Fig. 15. Results for the NACA 4412 airfoil at $R_C = 6 \times 10^6$ (a) trailing edge displacement thickness, (b) extent of flow separation on functions of angle of attack.

upstream in the case of a rough airfoil than in the case of a smooth airfoil, the trailing edge value is higher in the rough case with $C_{\ell\ max}$ consequently lowered. Figure 15b shows the extent of the trailing-edge separation as a function of the angle of attack and quantifies the earlier separation associated with the rough surface.

The NACA 23012 airfoil, like the NACA 4412, has camber and the results of the calculations are shown in Figs. 16 and 17. The lift and drag curves of Fig. 16 again demonstrate good agreement between the computations and measurements, and the drag curve is in even better agreement than that for the NACA 4412. Figure 17a shows the value of dimensionless displacement thickness at the trailing edge and Fig. 17b the trailing edge separation both as a function of the angle of attack. The slope of the trailing-edge separation curve of Fig. 17b at 11° angle of attack suggests that, with the rough surface, separation would occur over a very large portion of the airfoil if the angle of attack were increased.

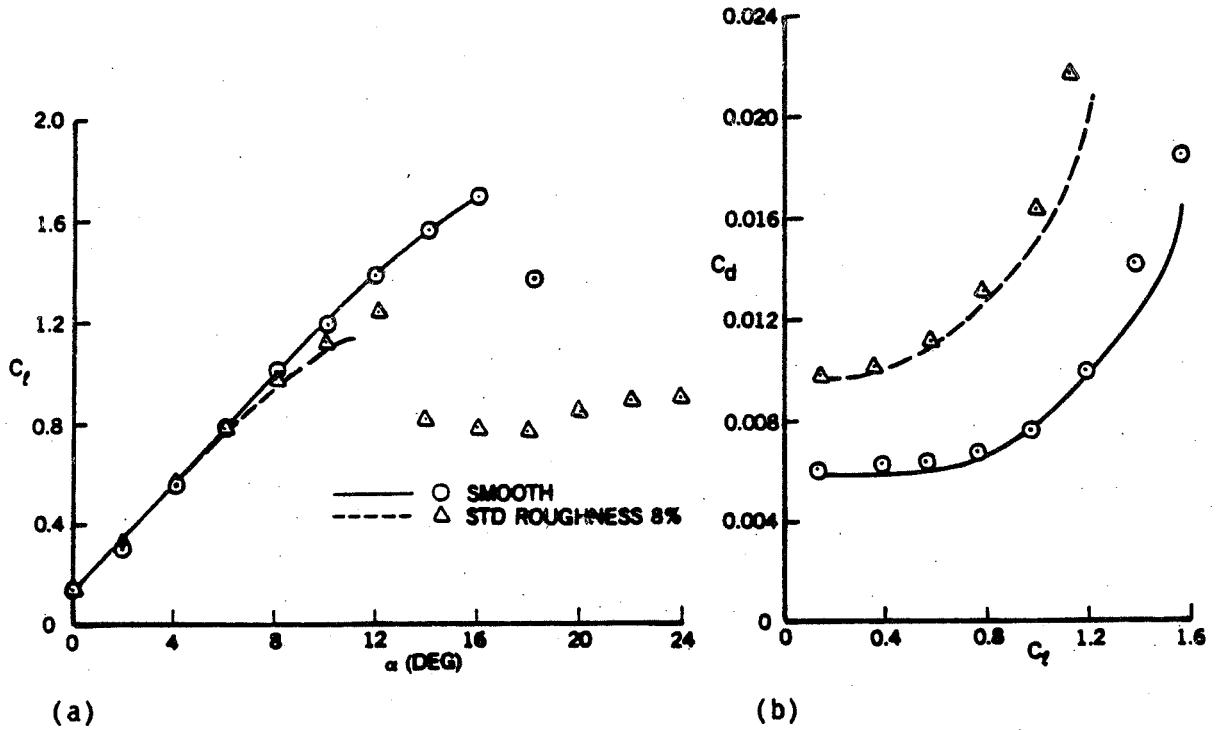

(a) (b)

Fig. 16. Comparison of calculated and experimental results for the NACA 23012 airfoil at $R_C = 6 \times 10^6$.

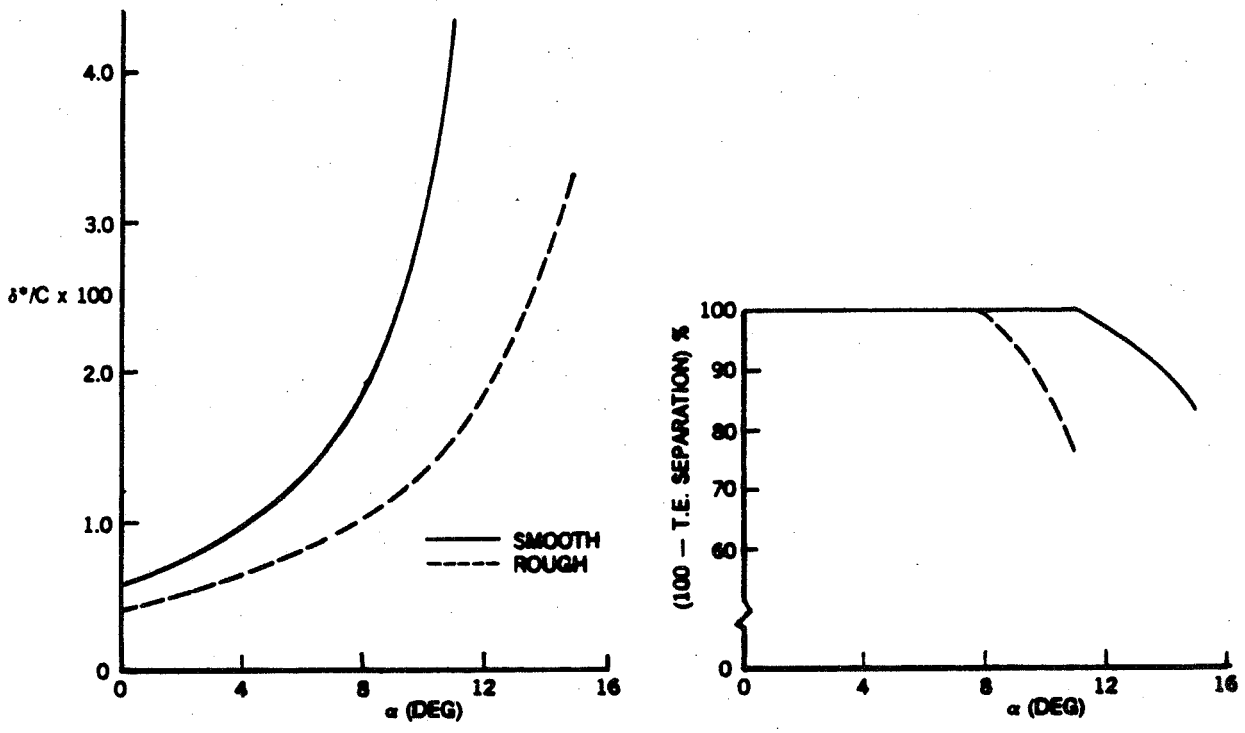

(a) (b)

Fig. 17. Results for the NACA 23012 airfoil at $R_C = 6 \times 10^6$. (a) Trailing edge displacement, and (b) extent of flow separation as functions of angle of attack.

These results, together with the results shown in Fig. 18 for the NACA 0012 airfoil, quantify the extent to which the interactive boundary-layer method can represent the flows over airfoils with roughened surfaces. It is evident that the calculation method correctly represents this effect and the trends of the lift and drag curves. Where the effects of ice, rain or insect deposition can be regarded as roughness with an equivalent sand-grain value, similar results can be expected.

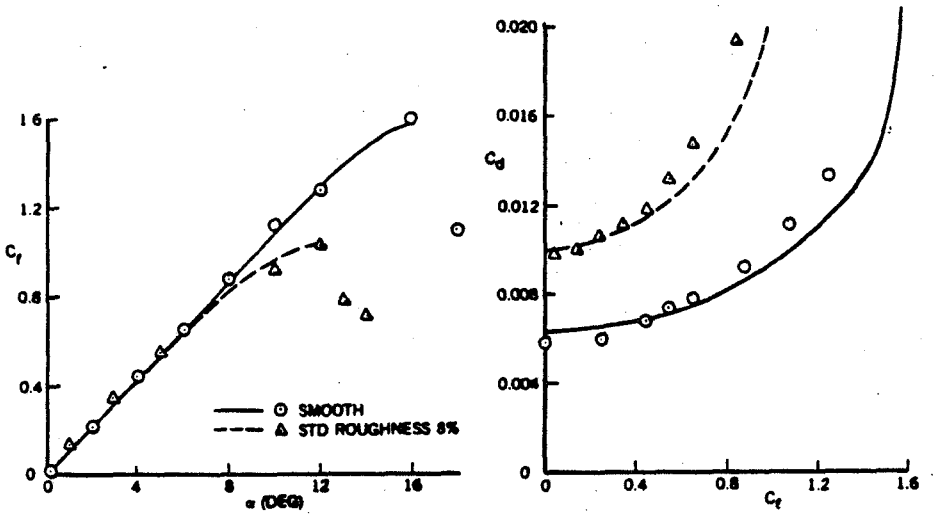

(a) (b)

Fig. 18. Comparison of calculated results for the NACA 0012 airfoil at $R_C = 6 \times 10^6$.

5.3 Iced Airfoil

This section presents results for airfoils with ice accretions large enough to change the shape of the leading edge. The results of the two calculation procedures are compared with the measurements of Bragg and Coirier [9], obtained with an NACA 0012 airfoil at a Reynolds number of 1.4×10^6 and at angles of attack up to 10 degrees. A large change in the leading edge was arranged with a wooden attachment to represent the shape of a typical glaze-ice formation. The calculations with the TLNS equations were performed by Potapcynk [52] with the ARC2D code and the grid of 253 x 64 nodes shown in Fig. 19.

The lift and drag coefficients computed with the ARC2D code are shown in Fig. 20 as functions of angle of attack. As can be seen, the results agree well with the measurements up to an angle of attack slightly smaller than

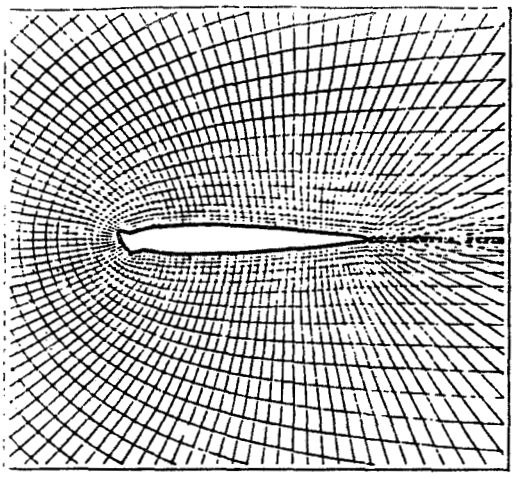

Fig. 19. Grid used in the TLNS code for the NACA 0012 iced airfoil at $\alpha = 10°$.

that of maximum lift. At this angle, as in the case of "clean" airfoils, the computed lift coefficient does not agree as well but the drag coefficient agrees remarkably well with the data.

Before we present the results obtained with the interactive boundary-layer approach, it is useful to comment on the inviscid method and to discuss the role of the ice on the boundary-layer calculations. In the latter case the ice accretion can drastically change the pressure

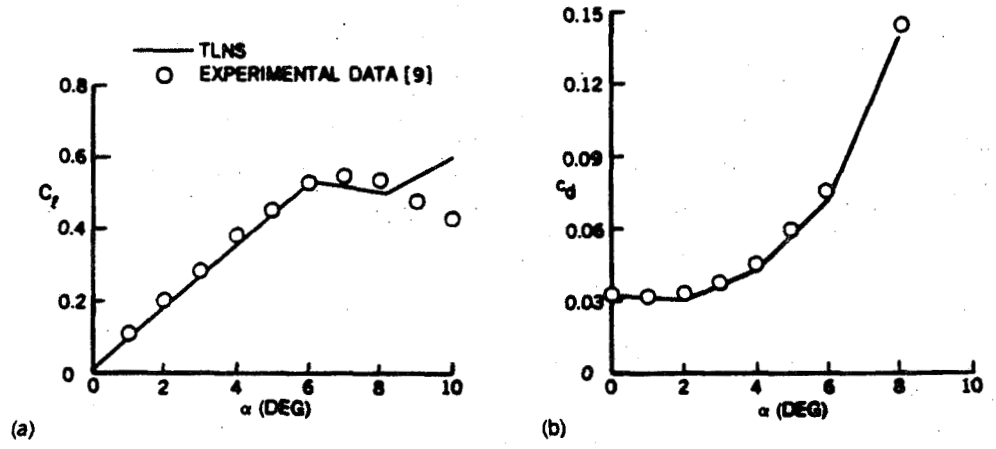

Fig. 20. Computed (a) lift and (b) drag coefficients for the iced airfoil of Ref.9.

distribution near the leading edge and can cause the viscous flow calculations to break down.

The interactive boundary-layer results presented in the previous two sections were obtained with inviscid flow computed by the conformal-mapping technique developed by Halsey [32]. While this technique gives excellent results for clean and rough airfoils, preliminary studies showed that it was less satisfactory for iced airfoils of interest. The reason appears to be that the conformal mapping uses up to 250 points equally spaced around the circle into which the airfoil is mapped and these are not

sufficiently concentrated at the leading edge to represent a complicated shape such as that of the accumulated ice. For this reason, attention was directed to a panel method [33] in which the airfoil is defined by a set of points in the physical plane, which would allow the concentration of points in the leading-edge region and to verify graphically that the ice shape has been adequately represented. Neighboring points on the airfoil are connected by straight-line panels so that, in a sense, the airfoil is approximated by a high-order inscribed polygon. Each panel has both source density and vorticity distributed along it with panel vorticity strengths set equal so that the vorticity is defined by a single parameter, total strength, which is adjusted to satisfy the Kutta condition. The source strengths, however, have independent values on each panel and these are adjusted, by solving a set of simultaneous linear equations, to satisfy the normal-velocity boundary condition at the midpoints of the panels. In the strictly inviscid case this condition requires that the total normal velocity, freestream plus body sources and vortices, should vanish. When the boundary layer is simulated, the desired normal velocity is finite and equals the derivative along the surface of the product of tangential velocity and displacement thickness. It is known that this surface blowing distribution displaces the dividing streamline outward from the surface of the airfoil to the location of the displacement surface. Experience has shown that best results are obtained when the surface pressures are calculated and the Kutta condition is applied on the displacement surface, rather than on the surface panels.

In general, boundary-layer calculations are rather sensitive to rapid variations in the external velocity distribution. In order to maintain computational accuracy and avoid early breakdown of the solutions in regions of steep adverse pressure gradients, it is necessary to take fine steps in the streamwise direction. For airfoils with large ice accretions, however, it is further necessary to reduce the sensitivity of the boundary-layer calculations to the pressure distribution. In the extension of the interactive boundary-layer approach of Cebeci et al. to iced airfoils, this is accomplished by using a continuation method in which the prescribed ice shape is introduced into the calculations gradually. Figure 21 shows a sketch of the iced airfoil in which the ice shape changes in increments of n ranging from 0 to 1 with n = 0 corresponding to the clean airfoil and n = 1 to the airfoil with the prescribed ice shape of Ref. 9.

In performing the interactive boundary-layer calculations for iced airfoils, unlike the procedure used for clean and rough airfoils, the viscous flow calculations were performed only up to the trailing edge and did not include the influence of the wake, thus restricting the accuracy of the solutions at high angles of attack. Studies are under way to remove this restriction.

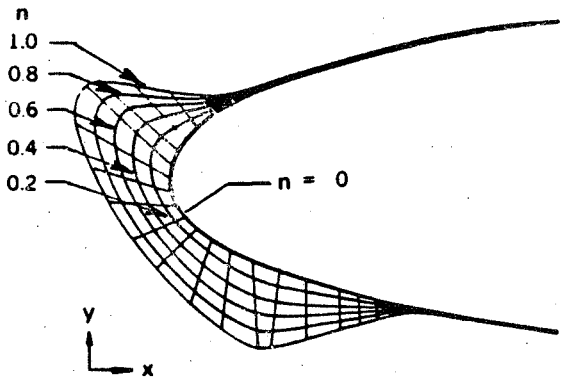

Fig. 21. Ice shapes used in the continuation method of the interactive boundary-layer scheme; n = 1 corresponds to the prescribed shape.

At first the calculations were performed for the clean airfoil (n = 0) at α = 0. After convergence, the ice shape was introduced into the calculations by taking the value of n equal to 0.4 and iterating the solutions until convergence. Subsequent calculations were then made for new values of n equal to 0.5, 0.6, 0.7, 0.8, 0.85, 0.90, 0.925, 0.950, 0.975 and 1.0. Once a complete converged solution for α = 0 was obtained, the calculations for another angle of attack were performed for n = 1 by initially computing the pressure distribution for the new α for the blowing velocity of the iced airfoil at α = 0. With each solution of the boundary-layer equations, a new blowing velocity was computed to obtain a new pressure distribution, and, as before, this procedure was continued until convergence. At small angles of attack, it was sufficient to choose the angle of attack increments, $\delta\alpha$, to be around 0.50°; at higher angles of attack, especially at conditions approaching stall, $\delta\alpha$ had to be chosen smaller, becoming around 0.1° for α's between 5° and 6°.

Figure 22 shows the inviscid external velocity distribution near the leading edge of the airfoil shown in Fig. 21. As can be seen, the inviscid velocity distribution differs significantly with and without ice: the clean airfoil has a favorable pressure gradient followed by an almost zero pressure gradient whereas the iced airfoil has a severe adverse pressure gradient after a short initial region of favorable pressure gradient. For both surfaces the rapid flow deceleration is followed by a gentle favorable

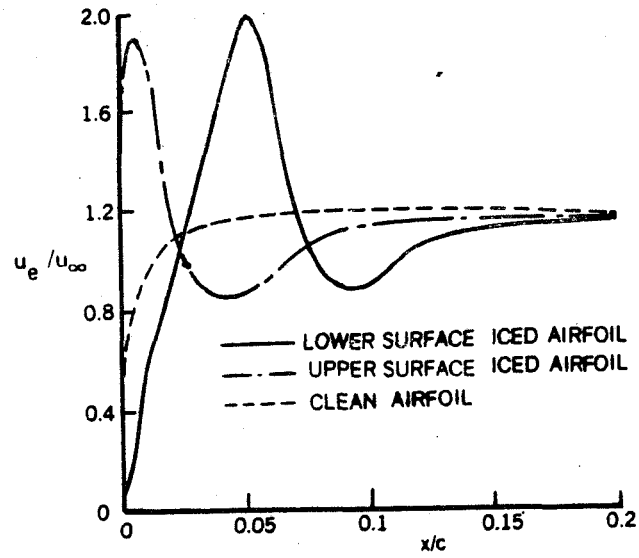

Fig. 22. Inviscid u_e/u_∞ distributions for iced and clean NACA 0012 airfoil at $\alpha = -0.15°$.

pressure gradient and the locations of possible flow separation can be easily identified.

The results shown in Figs. 23 to 27 correspond to interactive boundary-layer calculations obtained for the inviscid velocity distribution of Fig. 22 after several boundary-layer sweeps along the airfoil. As in the case of a clean airfoil, the calculations were started at the stagnation point of the airfoil. The leading-edge results of Fig. 23 show that the computed external velocity distribution changes drastically with each sweep from that predicted by inviscid flow theory, but the location of flow separation for each surface remains essentially unchanged. The calculations, see also Fig. 24, indicate a 10-percent separation bubble for the upper surface and a 25-percent separation bubble for the lower surface. Unlike the separation point, the reattachment point moves upstream with each sweep, but the difference in reattachment points becomes smaller with increase in the number of sweeps. The velocity profiles on the upper surface of the airfoil, Fig. 25, show that the extent of flow separation is large and that the present method is still able to cope well with it.

Perhaps the biggest surprise in the interactive flow calculations is the behavior of the displacement thickness distribution on the airfoil. Since the incidence angle is practically zero and the airfoil is symmetrical, the displacement-thickness distributions on both surfaces are the same for

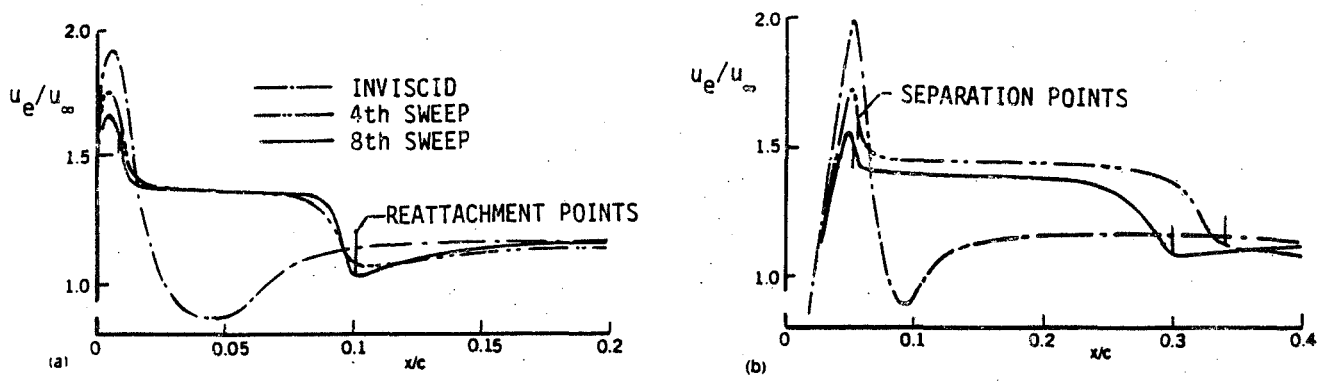

Fig. 23. Variation of external velocity distribution on iced NACA 0012 airfoil with each boundary-layer sweep for α = -0.15° and R_c = 1.5 x 10^6, (a) upper surface, (b) lower surface.

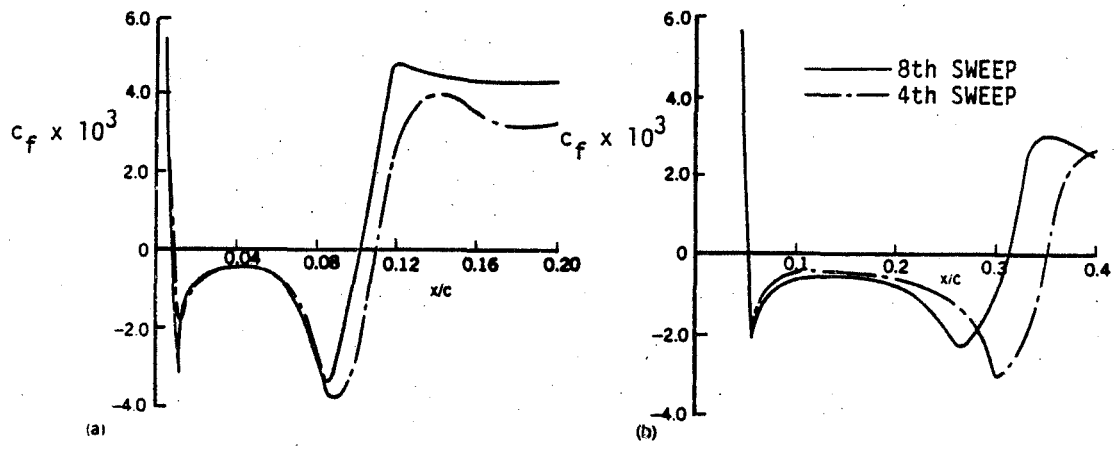

Fig. 24. Variation of local skin-friction coefficient distribution on iced NACA 0012 airfoil with each boundary-layer sweep for α = -0.15° and R_c = 1.5 x 10^6, (a) upper surface, (b) lower surface.

the clean airfoil. Its magnitude at the trailing edge is approximately one-half percent of the airfoil chord, which is relatively small and has a very small effect on the overall pressure distribution. In the case of the iced airfoil, the flow separation due to ice alters the displacement thickness distribution on the airfoil, as shown in Fig. 26. The lower surface has a large separation bubble which causes the magnitude of the displacement thickness at the trailing edge to be about two percent of the airfoil chord. The upper surface has a smaller separation bubble and, as a result, the displacement thickness at the trailing edge is about one percent of the airfoil chord. This difference in the magnitudes of displacement thicknesses due to ice affects the pressure distribution and leads to a higher drag.

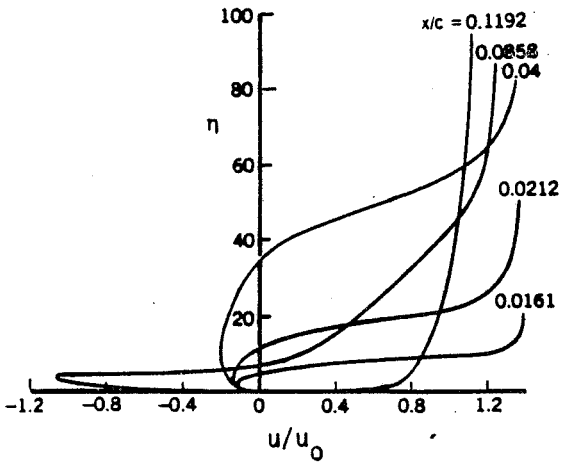

Fig. 25. Velocity profiles on the upper surface of iced NACA 0012 airfoil, α = 0.15° and R_c = 1.5 x 10^6.

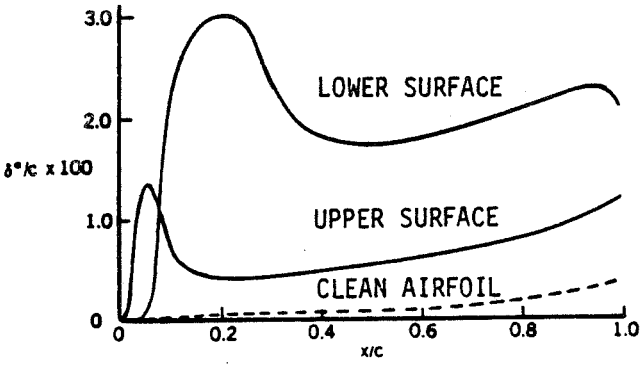

Fig. 26. Displacement thickness distributions for clean and iced NACA 0012 airfoil at α = -0.15° and R_c = 1.5 x 10^6.

To provide further insight into the behavior of the solutions, calculations were performed in which inviscid and viscous flow equations were solved successively. That is, rather than making several sweeps along the airfoil for a given pressure distribution, one boundary-layer sweep was made and the inviscid flow was updated with the blowing velocity v_n computed by the boundary-layer method. The results in Fig. 27 correspond to the variation of the external velocity distribution on both surfaces of the airfoil with each cycle and show that the separation bubble of the previous calculations becomes smaller and almost equal to that on the upper surface when the initial inviscid solution is updated. In both cases, the separation and reattachment locations of the bubbles remain essentially unchanged after four cycles. As expected, the external velocity in the separated region is uniform and decreases sharply near the reattachment point in accord with the behavior of separating and reattaching flows. The separation bubble is roughly ten percent of the chord, which is in agreement with the experimental result of Bragg and Coirier. The lift is nearly independent of the viscous effects for this angle of attack but the total drag coefficient requires the solution of the boundary-layer equations and the result is different from that for a clean airfoil.

Figures 28 to 30 show additional results for the same iced airfoil. Comparison of calculated lift and drag coefficients for a range of angles

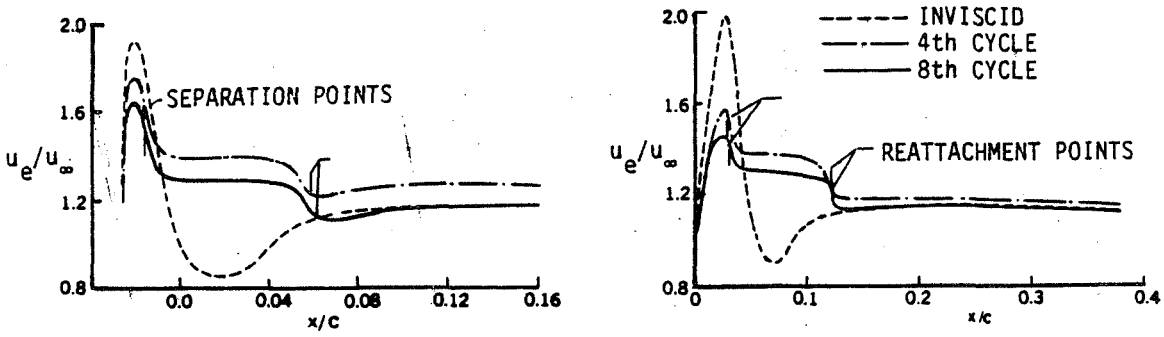

Fig. 27. Variation of external velocity distribution with each cycle for iced NACA 0012 airfoil at $\alpha = -0.15°$, $R_c = 1.5 \times 10^6$.

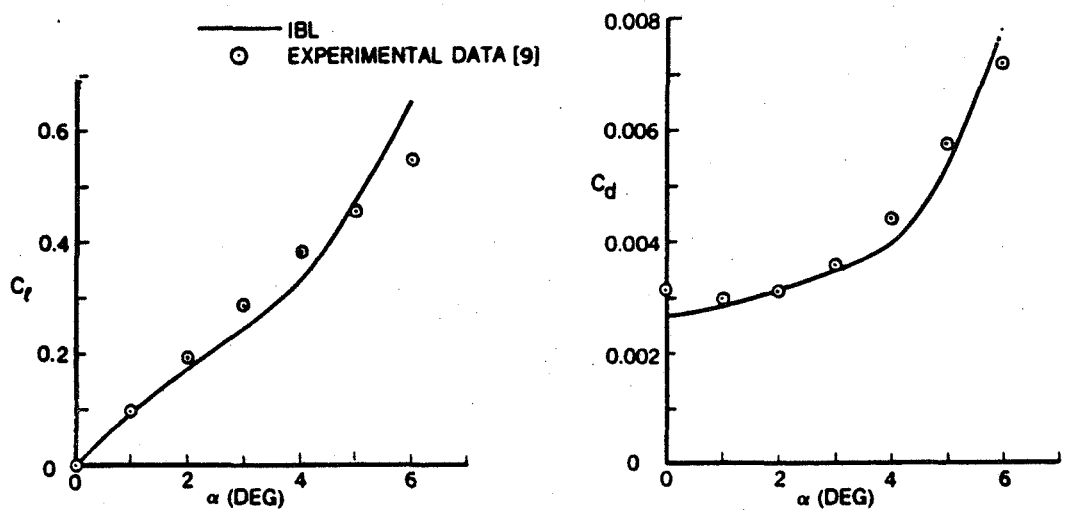

Fig. 28. Comparison of calculated and experimental results for the iced NACA 0012 airfoil, $R_c = 1.5 \times 10^6$.

of attack up to stall ($\alpha \approx 6°$) indicate that in general there is good agreement with data. As expected, however, the behavior of the computed lift coefficients need improvement. While the agreement at lower angles of attack is satisfactory, it deteriorates with increasing angle of attack due to the neglect of the wake effect. Figures 29 and 30 show the results for $\alpha = 6°$. As can be seen from Fig. 29, at this angle of attack, there are substantial differences between the inviscid and viscous velocity distribution. Perhaps the most remarkable aspect of the calculations is the behavior of the viscous flow solutions on the upper surface of the airfoil shown in Fig. 30a. The calculations indicate approximately twenty-percent-chord leading-edge separation followed by fifteen percent marginally

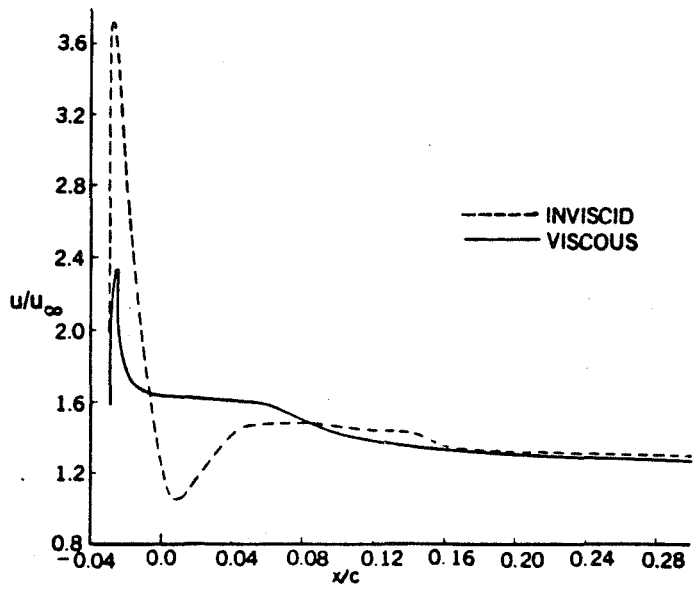

Fig. 29. Comparison of inviscid and viscous velocity distributions for the upper surface of the NACA 0012 iced airfoil at $\alpha = 6°$.

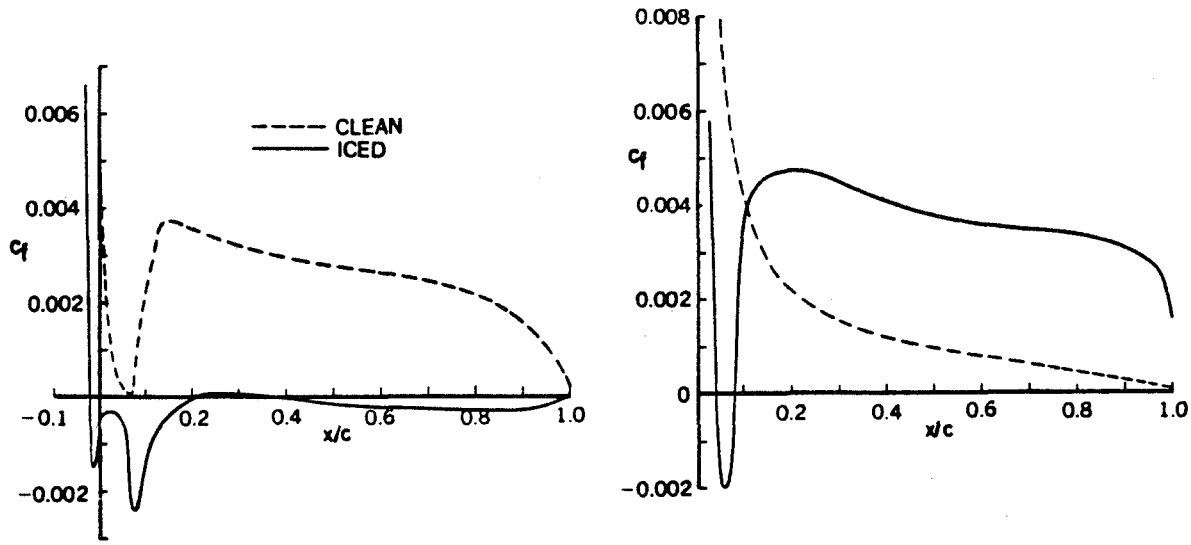

Fig. 30. Variation of the local skin-friction coefficient c_f on the (a) upper, and (b) lower surfaces of the clean and iced NACA 0012 airfoil at $\alpha = 6°$.

attached flow and sixty-five percent separated flow up to the trailing edge. It is possible that with the inclusion of wake effects, the extent of the flow separation on the airfoil will decrease. Nevertheless, from a numerical point of view, the calculations are able to cope well with such rather extensive flow separation.

Acknowledgment: This work was partially supported by the National Science Foundation grant MEA 0818565 and by the NASA Lewis grant NAG3-601.

6.0 References

1. Rhode, R.V.: Some Effects of Rainfall on Flight Airplanes and on Instrument Indications. NACA TN 803, April 1941.
2. Dunham, R.E., Bezos, G.M. and Gentry G.L., Jr.: Two-Dimensional Wind Tunnel Tests of a Transport-Type Airfoil in a Water Spray. AIAA Paper 85-0258, Jan. 1985.
3. Hansman, R.J., Jr. and Barsotti, M.F.: Surface Wetting Effects on a Laminar Flow Airfoil in Simulated Heavy Rain. J. Aircraft 22, 1049-1053, 1985.
4. Haines, P. and Luers, J.: Aerodynamic Penalties of Heavy Rain on Landing Airplanes. J. Aircraft 20, 111-119, 1983.
5. Coleman, W.S.: The Characteristics of Roughness from Insects as Observed for Two-Dimensional, Incompressible Flow Past Airfoils. J. Aerospace Sci. 264, 1959.
6. Gray, V.H. and von Glahn, U.H.: Aerodynamic Effects Caused by Icing of an Unswept NACA 65A004 Airfoil. NACA TN 4155, 1957.
7. Korhan, K.D., Dadone, L. and Shaw, R.J.: Performance Degradation of Helicopter Rotor Systems in Forward Flight Due to Rime Ice Accretion. AIAA Paper 83-0029, 1983.
8. Bragg, M.B. and Gregorek, G.M.: Wind-Tunnel Investigation of Airfoil Performance Degradation Due to Icing. AIAA Paper 82-0582, March 1982.
9. Bragg, M.B. and Coirier, W.J.: Detailed Measurements of the Flowfield in the Vicinity of an Airfoil with Glaze Ice. AIAA Paper 85-0409, Jan. 1985.
10. Korkan, K.D., Cross, E.J., Jr. and Cornell, C.C.: Experimental Aerodynamic Characteristics of an NACA 0012 Airfoil with Simulated Ice. J. Aircraft 22, 130-134, 1985.
11. Belte, D.: In-Flight Ice Accretion Characteristics of Rotor Blade Airfoil Sections. AIAA Paper 87-0176, Jan. 1987.
12. Cebeci, T., Clark, R.W., Chang, K.C., Halsey, N.D. and Lee, K.: Airfoils with Separation and the Resulting Wakes. J. Fluid Mech. 163, 323-347, 1986.
13. Shaw, R.J.: NASA's Aircraft Icing Analysis Program, NASA TM 88791, 1986.

14. Shaw, R.J.: A Review of Techniques for Predicting Airfoil Performance in Icing. AIAA Paper 87-0028, Jan. 1987.
15. Korkan, K.D., Dadone, L. and Shaw, R.J.: Performance Degradation of Propeller/Rotor Systems Due to Rime Ice Accretion. AIAA Paper 82-0286, Jan. 1982.
16. Korkan, K.D., Dadone, L. and Shaw, R.J.: Performance Degradation of Helicopter Rotor Systems in Forward Flight Due to Rime Ice Accretion. J. Aircraft 22, 713-718, 1985.
17. Miller, T.L.: Analytical Determination of Propeller Performance Degradation Due to Ice Accretion. NASA CR-175092, 1986.
18. Flemming, R.J. and Lednicer, D.A.: High Speed Ice Accretion on Rotorcraft Airfoils. NASA CR-3910, 1985.
19. Gregorek, G.M., et al: NASA Twin Otter Flight Test Program - Comparison of Flight Results with Analytic Theory. SAE Paper No. 850924, Apr. 1985.
20. Bragg, M.B., Gregorek, G.M. and Lee, J.D.: Airfoil Aerodynamics in Icing Conditions. J. Aircraft 23, 76-81, 1986.
21. Brumby, R.E.: Wing Surface Roughness: Cause and Effect. D.C. Flight Approach, No. 32, 1979.
22. Gray, V.H.: Prediction of Aerodynamic Penalties Caused by Ice Formation on Various Airfoils. NASA TN D-2166, 1964.
23. Bragg, M.B.: Rime Ice Accretion and Its Effect on Airfoil Performance. NASA CR-165599, 1982.
24. Cebeci, T., Stewartson, K. and Whitelaw, J.H.: Calculation of Two-Dimensional Flow Past Airfoils. In Numerical and Physical Aspects of Aerodynamic Flows II (ed. T. Cebeci) 1-40, Springer-Verlag, N.Y., 1984.
25. Cebeci, T. and Whitelaw, J.H.: Calculation Methods for Aerodynamic Flows - A Review. In Numerical and Physical Aspects of Aerodynamic Flows III (ed. T. Cebeci) 1-22, Springer-Verlag, N.Y., 1986.
26. Pulliam, T.H.: Euler and Thin-Layer Navier-Stokes Codes: ARC2D, ARC3D. Notes for Computational Fluid Dynamics User's Workshop. The University of Tennessee Space Institute, Tullahoma, Tenn., 1984.
27. Mehta, U., Chang, K.C. and Cebeci, T.: Relative Advantages of Thin-Layer Navier-Stokes and Interactive Boundary-Layer Procedures. NASA TM-86778, 1985.

28. Mehta, U. and Lomax, H.: Reynolds Averaged Navier-Stokes Computations of Transonic Flows - The State-of-the-Art, Transonic Aerodynamics, (ed. D. Nixon), Progress in Astronautics and Aeronautics, Vol. 81, 1982, p. 297.

29. Blottner, F.G.: Significance of the Thin-Layer Navier-Stokes Approximation. In Numerical and Physical Aspects of Aerodynamic Flows, III (ed. T. Cebeci), p. 184-197, Springer-Verlag, 1986.

30. Beam, R. and Warming, R.F.: An Implicit Factored Scheme for the Compressible Navier-Stokes Equations. AIAA J., Vol. 16, 1978, p. 393.

31. Mehta, U., Chang, K.C. and Cebeci, T.: A Comparison of Interactive Boundary Layer and ThinLayer Navier-Stokes Procedures. In Numerical and Physical Aspects of Aerodynamic Flows III (Ed. T. Cebeci), p. 198-215, Springr-Verlag, N.Y., 1986.

32. Halsey, N.D.: Potential Flow Analysis of Multielement Airfoils Using Conformal Mapping. AIAA J., Vol. 17, 1979, p. 1281.

33. Hess, J.L. and Smith, A.M.O.: Calculation of Potential Flow About Arbitrary Bodies. Progress in Aeronautical Sciences Series, Vol. 8, Pergamon Press, 1966.

34. Cebeci, T. and Smith, A.M.O.: Analysis of Turbulent Boundary Layers. Academic Press, 1974.

35. Cebeci, T. and Clark, R.W.: An Interactive Approach to Subsonic Flows with Separation. In Numerical and Physical Aspects of Aerodynamic Flows, II (Ed. T. Cebeci), p. 193-204, Springer-Verlag, N.Y., 1984.

36. Bradshaw, P., Cebeci, T. and Whitelaw, J.H.: Engineering Calculations of Turbulent Flows, Academic Press, 1981.

37. Cebeci, T.: Separated Flows and Their Representation by Boundary-Layer Equations. Mech. Eng. Rept. ONR-CR215-234-2, California State University, Long Beach, 1976.

38. Cebeci, T. and Chang, K.C.: Calculation of Incompressible Rough-Wall Boundary-Layer Flows. AIAA J., Vol. 16, 1978, p. 730.

40. Wadcock, A.J.: Flying-Hot-Wire Study of Two-Dimensional Turbulent Separation on an NACA 4412 Airfoil at Maximum Lift. Ph.D. Thesis, Cal. Tech., Pasadena, CA, 1978.

41. Coles, D. and Wadcock, A.J.: Flying-Hot-Wire Study of Flow Past an NACA 4412 Airfoil at Maximum Lift. AIAA J., Vol. 17, 1979, p. 321.

42. Pinkerton, R.M.: Calculated and Measured Pressure Distributions Over the Midspan Section of the NACA 4412 Airfoil. NACA Rept. No. 563, 1936.

43. Michel, R.: Etude de la transition sur les profiles d'aile; establishment d'un critere de determination de point de transition et calcul de la trainee de profile incompressible. ONERA Report 1/1578A, 1951.

44. Cebeci, T. and Bradshaw, P.: Physical and Computational Aspects of Convective Heat Transfer. Springer-Verlag, N.Y., 1984.

45. Abbott, J.H. and von Doenhoff, A.E.: Theory of Wing Sections, Dover, 1959.

46. Gregory, N. and O'Reilly, C.L.: Low-Speed Aerodynamic Characteristics of NACA 0012 Airfoil Section, Including the Effects of Upper-Surface Roughness Simulating Hoar Frost. NPL Aero Rept. 1308, 1970.

47. Loftin, L.K., Jr. and Smith, H.A.: Aerodynamics of 15 NACA Airfoil Sections at Seven Reynolds Numbers from 0.7 x 10^6 to 9 x 10^6. NACA TN 1945, 1949.

48. McGhee, R.J., Beasley, W.D. and Somers, D.M.: Low-Speed Aerodynamic Characteristics of a 13-Percent Thick Airfoil Section Designed for General Aviation Application. NASA TM 72697, 1977.

49. Cebeci, T. Wang, G.S., Chang, K.C. and Choi, J.: Recent Developments in the Calculation of Flow Over Low Reynolds Number Airfoils. Proceedings of the Intern. Conf. on Aerodynamics at Low Reynolds Numbers, Royal Aero. Soc., London, 16-17 Oct. 1986.

50. Abbott, I.H., von Doenhoff, A.E. and Stivers, L.S.: Summary of Airfoil Data. NACA Rept. No. 824, 1945.

51. Smith, A.M.O. and Kaups, K.: Aerodynamics of Surface Roughness and Imperfections. SAE Paper 680198, Apr. 1968.

52. Potapcynk, M.: Numerical Analysis of a NACA 0012 Airfoil with Leading Edge Ice Accretions. AIAA Paper 87-0101, Jan. 1987.